

Probing All-Solid-State Batteries with Real-Time Synchrotron and Neutron Techniques

Suzhe Liang, Yipeng Sun^{}, Ya-Jun Cheng, Stephan V. Roth, Peter Müller-Buschbaum, Longsheng Cao, Jian Peng, Shuo Wang, Xueliang Sun^{*}, Changhong Wang^{*}*

Dr. S. Liang, Prof. Y. Sun, Prof. J. Peng, Prof. S. Wang, Prof. X. Sun, Prof. C. Wang
Eastern Institute for Advanced Study, Ningbo Institute of Digital Twin, Eastern Institute of Technology, Ningbo 315200, China

Dr. S. Liang, Prof. Y. Sun, Prof. J. Peng, Prof. S. Wang, Prof. X. Sun, Prof. C. Wang
Zhejiang Key Laboratory of All-Solid-State Battery, Ningbo Key Laboratory of All-Solid-State Battery, Ningbo 315200, China

Dr. S. Liang, Prof. L. Cao
School of Chemistry and Materials Science, University of Science and Technology of China, Hefei 230026, China

Prof. Y.-J. Cheng
College of Renewable Energy, Hohai University, 1915 Hohai Avenue, Changzhou 213200, China
Ningbo Institute of Materials Technology & Engineering, Chinese Academy of Sciences, Ningbo 315201, China

Prof. S. V. Roth
Deutsches Elektronen-Synchrotron DESY, Notkestr. 85, 22607 Hamburg, Germany
KTH Royal Institute of Technology, Department of Fibre and Polymer Technology, Teknikringen 56-58, SE-100 44 Stockholm, Sweden

Prof. P. Müller-Buschbaum
Technical University of Munich, TUM School of Natural Sciences, Department of Physics, Chair for Functional Materials, James-Franck-Str. 1, 85748 Garching, Germany

Prof. L. Cao
State Key Laboratory of Bioinspired Interfacial Materials Science, Suzhou Institute for Advanced Research, University of Science and Technology of China, Suzhou 215123, China

^{*}Corresponding author E-mail:

Yipeng Sun: ypsun@eitech.edu.cn

Xueliang Sun: xsun@eitech.edu.cn

Changhong Wang: cwang@eitech.edu.cn

Abstract

All-solid-state batteries (ASSBs) are emerging as a next-generation energy storage technology, offering enhanced safety and energy density compared to conventional lithium-ion batteries. However, critical challenges related to material design and interfacial stability hinder their practical deployment. Advanced synchrotron X-ray and neutron-based techniques have become indispensable for probing the structural, chemical, and morphological evolutions within ASSBs across multiple length scales and under realistic operating conditions. This review provides a comprehensive and critical overview of recent *in situ* and *operando* studies of ASSBs enabled by synchrotron and neutron sources. The discussion is organized by the key components and interfaces of ASSBs, highlighting how these techniques elucidate dynamic processes during battery operation. Fundamental principles of the characterization methods are introduced, along with perspectives on future directions. This work aims to guide the rational design of high-performance ASSBs by showcasing how cutting-edge characterization advances can address longstanding challenges.

Keywords: All-solid-state batteries; *In situ* and *operando* characterization techniques; Synchrotron radiation source; Neutron source

Abbreviation List

ALD	atomic layer deposition	LSC	Li_3ScCl_6
ASSB	all-solid-state battery	LSPS	$\text{Li}_{10}\text{SnP}_2\text{S}_{12}$
ASSLMB	all-solid-state lithium metal battery	NASICON	Na super ion conductor
ASSLSB	all-solid-state lithium-sulfur battery	NCM	lithium-nickel-cobalt-manganese oxides
ASSSB	all-solid-state sodium battery	ND	neutron diffraction
CAM	cathode active material	NDP	neutron depth profile
CCD	critical current density	NI	neutron imaging
CEI	cathode electrolyte interface	NR	neutron reflectometry
DoD	degree of discharge	NT	neutron tomography
EDXRD	energy-dispersive X-ray diffraction	NVP	$\text{Na}_3\text{V}_2(\text{PO}_4)_3$
EXAFS	extended X-ray absorption fine structure	PEO	poly(ethylene oxide)
GISAXS	grazing-incidence small-angle X-ray scattering	QENS	quasi-elastic neutron scattering
GIWAXS	grazing-incidence wide-angle X-ray scattering	SANS	small-angle neutron scattering
HAXPES	hard X-ray photoelectron spectroscopy	SAXS	small-angle X-ray scattering
LAGP	$\text{Li}_{1+x}\text{Al}_x\text{Ge}_{2-x}(\text{PO}_4)_3$	SDD	sample-to-detector distance
LELIB	liquid electrolyte lithium-ion battery	SLD	scattering length density
LGPS	$\text{Li}_{10}\text{GeP}_2\text{S}_{12}$	SSE	solid-state electrolyte
LGSSI	$\text{Li}_{6.6}\text{Ge}_{0.6}\text{Sb}_{0.4}\text{S}_5\text{I}$	SXTM	scanning transmission X-ray microscopy
LIB	lithium-ion battery	WAXS	wide-angle X-ray scattering
LIC	Li_3InCl_6	XANES	X-ray absorption near-edge structure
LLZO	$\text{Li}_7\text{La}_3\text{Zr}_2\text{O}_{12}$	XAS	X-ray absorption spectroscopy
LMO	Li_2MnO_3	XCT	X-ray computer tomography
LNO	LiNbO_x	XPS	X-ray photoelectron spectroscopy
LPS	Li_3PS_4	XRD	X-ray diffraction
LPSC	$\text{Li}_6\text{PS}_5\text{Cl}$	XRR	X-ray reflectivity

1. Introduction

The accelerating global transition toward a low-carbon economy has intensified the demand for safe, high-performance, and sustainable energy storage technologies.^[1-3] Rechargeable batteries, as a cornerstone of this transition, must meet increasingly complex and stringent performance requirements across a wide range of applications—from portable electronics to electric vehicles and large-scale energy storage systems. Conventional lithium-ion batteries (LIBs), though highly successful over the past three decades, are nearing their performance limits in terms of energy density, safety, and durability,^[4-8] raising concerns about their ability to meet future needs.

All-solid-state batteries (ASSBs) have emerged as a promising next-generation energy storage technology, offering significant advantages for applications ranging from portable electronics to electric vehicles and grid-scale systems.^[9-10] Unlike traditional LIBs that rely on flammable liquid electrolytes, ASSBs employ solid electrolytes to mediate lithium-ion transport, enabling higher energy density, superior safety, wider operating temperature ranges, and improved thermal and mechanical stability.^[11-12] Despite these benefits, ASSBs face formidable challenges, including high interfacial resistance, chemical and mechanical degradation, and lithium dendrite growth—particularly at solid–solid interfaces—which critically impair performance and long-term stability.^[11, 13] Addressing these issues requires a fundamental understanding of the underlying physicochemical processes, particularly under operating conditions. In this context, *in situ* and *operando* characterization techniques have gained increasing attention. Generally, *in situ* measurements are conducted under conditions that mimic the working environment of the battery but may not involve simultaneous electrochemical operation, whereas *operando* measurements are performed during actual electrochemical cycling, thereby directly correlating structural or chemical changes with electrochemical performance. By utilizing advanced synchrotron X-ray and neutron-based methods, researchers can probe the evolution of materials and interfaces in real time and under realistic electrochemical environments.^[14-16] These techniques, based on interactions between incident beams and matter, offer diverse physical and chemical insights across spatial and temporal scales, and have become indispensable tools for investigating complex phenomena in ASSBs.^[14, 17-22]

This review provides a timely and comprehensive summary of recent developments—primarily

over the past five years—in *in situ* and *operando* studies of ASSBs using synchrotron and neutron facilities. Unlike conventional reviews that categorize techniques by measurement principles, this article is organized around the key challenges faced by ASSBs. Through this problem-oriented structure, we highlight how specific characterization strategies are designed and implemented to address distinct bottlenecks in the development of ASSBs. We start this review by introducing fundamentals and challenges of ASSBs in section 2 and how synchrotron and neutron sources are operated and related characterization techniques in section 3. The subsequent sections provide in-depth and in-detail discussions on how the scientists/engineers design various *in situ* and *operando* characterization techniques at synchrotron and neutron sources to investigate and solve key challenges that appear at specific areas within ASSBs.

2. Fundamentals and Challenges of ASSBs

Generally, a typical ASSB consists of anode (with lithium metal being a popular candidate), solid-state electrolyte (SSE) as the separator, composite cathode layer made by cathode active material (CAM) and SSE (as catholyte), as illustrated in **Figure 1**. Due to solid-solid contacts, ASSB can avoid several drawbacks of conventional LIBs operating with liquid electrolyte, such as safety and energy density. However, such configuration also brings issues on both materials and interfaces that realistically limit the development of ASSBs to be a potential mass-market product. Despite the need for designed high-performance SSEs and electrode materials, interface-related issues are more complex and greatly influence the performance and lifespan of ASSBs.^[23] At anode side, volume expansion and dendrite growth of lithium metal are the most complicated problems, which can directly lead to the anode detachment and short-circuit of the cell. Besides, pore formation between SSE layer and lithium metal, along with the growth of solid-electrolyte interface mainly leads to reduced dynamics of lithium-ion transport. Furthermore, SSE degradation is also a serious issue due to the chemical and electrochemical instability towards lithium. At the cathode/SSE interfaces, high charge transfer resistance due to the solid-solid contact, interphase layer formation, and stress-induced contact loss are non-negligible issues. Moreover, for the bulk SSE materials, the poor air or moisture-stability for most SSEs severely hinders the development of ASSBs towards industrial production. During cell operation, crack propagation within the crumbly SSE bulk layer is highly

risky owing to the possibility of short-circuiting. Similarly, inside the composited cathode, the CAM/catholyte interfaces also suffer from contact loss and interfacial instability. Moreover, the high tortuosity of lithium-ion transport in the composited cathode deteriorates the performance of CAM owing to the characteristics of pathway for charge transfer. Based on the cell level, several critical questions are expected to be addressed for ASSBs, including (i) how to enhance the limited lithium-ion transport, (ii) how to decouple the electro-chemo-mechanical complexity, and (iii) how to prevent the potential safety risk.

Aiming to solve or alleviate these issues, significant efforts and various optimization strategies have been implemented, including material optimization, compositional design, interface engineering, and interfacial optimization. To guide the optimization strategies, the underlying mechanisms of interface or material evolution and failure are highly necessary to be understood fundamentally and comprehensively. Therefore, various characterization techniques for *in situ* (changing the environment for the sample, such as temperature, atmosphere, and pressure) and *operando* (in real working conditions/devices) probing the evolutions of buried materials and interfaces inside ASSBs have been developed in recent years.^[24-27] Notably, the techniques based on synchrotron radiation sources and neutron sources demonstrate their power in *in situ* and *operando* characterization of ASSBs, due to the wide range of probing scale (from Å to μm) and the diversity in various features of sample (crystalline structure, morphology, and chemical environment).^[15, 19-21, 28-31] In this review, we specifically focus on the studies of *in situ* and *operando* X-ray and neutron related characterization techniques at large-scale facilities for the investigation of key challenges and issues of ASSBs in the last five years.

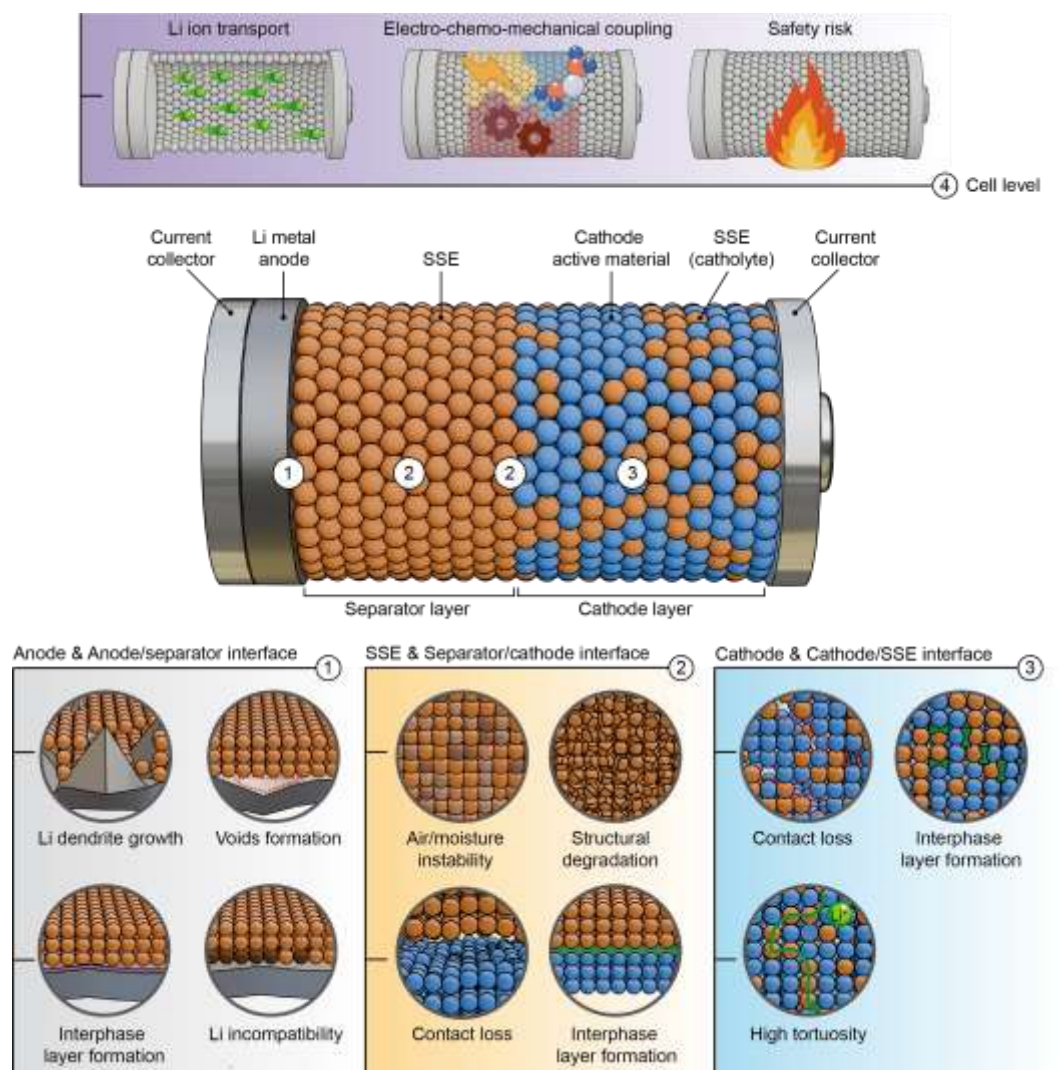


Figure 1. Illustrated configuration of a typical ASSB and key challenges at different regions/interfaces within ASSBs.

3. Synchrotron and Neutron sources and Techniques

Understanding how scientists and engineers generate high-energy X-ray and neutron beams is an important prelude to presenting their impactful applications on ASSBs for solving the key issues mentioned above. High-energy X-rays are produced by synchrotron radiation, which is based on classical electrodynamics: When a charged particle changes direction at relativistic speeds, it emits electromagnetic radiation in the form of a narrow cone tangent to its trajectory.^[32-33] **Figure 2A** illustrates the simplified construction of a typical synchrotron radiation facility. The electron beam is firstly generated by the electron gun located in the center of facility and then accelerated to approach the speed of light by the linear accelerator (linac).^[34-36] The accelerated electrons are then injected into the synchrotron booster, where their energy is increased by more than an order of magnitude,

reaching several GeV.^[37-39] The high-speed and high-energy electron beam is then transferred to the storage ring to maintain a stable energy level. The electron beam circulates around the storage ring with a circumference ranging from hundreds of meters to over a kilometer, which is guided by a series of magnets separated by straight sections. When the electrons are deflected through the magnetic field in a bending magnet, wiggler, or undulator, synchrotron radiation is produced, according to the electrodynamics.^[40-42] The generated synchrotron radiation X-rays are directed into experimental stations/hutches via beamlines, where they are manipulated for sample characterizations and studies. Compared to X-rays generated by conventional tubes, the synchrotron radiation X-rays offer significant advantages, including high brightness, broad tunability in energy and wavelength, high level of polarization, and short emission pulses.^[43-44] These unique properties make synchrotron radiation X-rays a powerful tool for probing the structure of matter across length scales ranging from sub-nanometers to millimeters. Therefore, they are widely applied in a variety of fields, such as condensed matter physics, materials science, biology, and medicine. In particular, synchrotron radiation X-rays are especially valuable for *in situ* and *operando* studies owing to the high brightness and short pulses duration.

Benefitting from the unique properties of synchrotron radiation X-rays, a wide range of advanced analysis techniques have been well developed at synchrotron beamlines. These techniques can be generally divided into three categories, i.e. scattering, spectroscopy, and imaging (as shown at the top right corner in the inset of Figure 2A).^[15] X-ray scattering/diffraction techniques, including X-ray diffraction (XRD), small-/wide-angle X-ray scattering (SAXS/WAXS), X-ray reflectivity (XRR), are used to reveal the sample's structure from atomic scale (crystalline structure) to microscale by detecting X-ray signals scattered by the object towards certain directions.^[45-48] The features may include crystalline planes of crystal (for XRD and WAXS analysis) and nano-/micro-structures of different samples (for SAXS analysis). Synchrotron-based X-ray scattering techniques have been extensively employed to determine the crystalline structures of newly synthesized materials and monitor crystalline structural evolutions of materials in ASSBs.^[49-51] X-ray spectroscopy techniques, such as X-ray photoelectron spectroscopy (XPS) and X-ray absorption spectroscopy (XAS), provide insights into elemental composition, chemical state, electronic structure, and geometry of matter based on the photoelectric effect (XPS) or absorption effect (XAS) when the

matter interacts with incident X-rays.^[52-54] In particular, XAS techniques, including X-ray absorption near-edge structure (XANES) and extended X-ray absorption fine structure (EXAFS), have gained great interests in investigating the physicochemical properties of materials in ASSBs, including valence state, coordination environment, and subtle geometrical distortions.^[55-61] X-ray imaging is a highly intuitive visualization method, with techniques such as X-ray computer tomography (XCT), which can be used to directly observe the internal structure of materials.^[62-66] XCT visualizes contrast in intensity resulting from X-rays that pass through the sample, which arises due to differences in absorption by different elements or other contrast mechanisms.^[67-68] Synchrotron-based XCT has also proven to be a very powerful tool for directly visualizing the buried features, such as pores and Li dendrites, of materials within ASSBs. Besides, an emerging advanced synchrotron-based technique, scanning transmission X-ray microscopy (STXM), has been a powerful tool in energy materials science. As a representative technique of soft X-ray spectromicroscopy, STXM combines the capabilities of X-ray microscopy and XAS, thus providing morphological, elemental, and chemical bonding information of the sample simultaneously.^[69-70] A concise comparison of key features of these synchrotron-based X-ray techniques is summarized in **Table 1**.

Table 1. Comparison of typical synchrotron-based X-ray characterization techniques.

Technique	Advantages	Limitations	Key insights
X-ray Diffraction (XRD)	<ul style="list-style-type: none"> - Gold standard for crystalline materials. - Quantitative phase analysis. - High-resolution for lattice parameters. 	<ul style="list-style-type: none"> - Requires long-range order (crystallinity). - Insensitive to amorphous phases. - Provides average structure of the bulk. 	Crystal structure: Phase identification, lattice parameters, crystallinity, strain, texture, atomic positions. (Å)
Wide-Angle X-Ray Scattering (WAXS)	<ul style="list-style-type: none"> - Suitable for the analysis of nanocrystalline and semi-crystalline materials. - Probes shorter-range order than standard XRD. 	<ul style="list-style-type: none"> - Less direct for full crystal structure than high-res XRD. - Data interpretation can be complex for disordered systems. 	Similar to XRD. Short-range order in liquids, glasses, polymers; nanocrystal size and shape. (Å)
Small-Angle X-Ray Scattering (SAXS)	<ul style="list-style-type: none"> - Probes structures from 1 nm to ~100-200 nm. - Works on amorphous and crystalline materials in solution or solid-state. - Statistically representative 	<ul style="list-style-type: none"> - Low structural specificity. - Requires contrast in electron density. - Model-dependent analysis. 	Nanoscale structure: Particle size, shape, distribution, pore size, specific surface area, nanoscale periodicity. (1-100 nm)
X-Ray	<ul style="list-style-type: none"> - Extreme surface 	<ul style="list-style-type: none"> - Requires Ultra-High 	Elemental composition,

Photoelectron Spectroscopy (XPS)	sensitivity. - Quantitative.	Vacuum. - Shallow probing depth (~10 nm). - Risk of beam damage to sensitive surfaces.	chemical state, and oxidation state of surfaces (top 1-10 nm). Empirical formula.
X-Ray Absorption Spectroscopy (XAS)	- Element-specific probe. - Does not require long-range order (works on crystals, glasses, solutions, surfaces).	- Model-dependent analysis (EXAFS). - Limited sensitivity to light elements/neighbors of similar Z. - Average bulk measurement (unless in microprobe mode).	Local electronic and geometric structure: oxidation state, coordination chemistry, bond distances, coordination numbers, species type (EXAFS/XANES).
X-Ray Computed Tomography (XCT)	- Non-destructive 3D imaging - Macroscopic field of view	- Resolution vs. Field-of-View trade-off. - Often requires contrast in attenuation. - Large data sets; complicated processing and analysis.	3D internal structure (morphology, cracks, pores, interfaces). Material composition and density variations. (μm -mm)
Scanning Transmission X-Ray Microscopy (STXM)	- Combines high spatial resolution with XAS chemical specificity. - Measurement in air or helium for wet/ambient samples. - High contrast for light elements (C, N, O).	- Slow acquisition (raster scanning). - Requires thin samples (< 1-2 μm for optimal contrast). - Risk of radiation damage due to high dose	Spectro-microscopy: Chemical mapping at the nanoscale based on XAS contrast. Morphology and composition. (30-50 nm)

There are currently two methods for generating neutron beams for scientific studies, neutron reactors and spallation neutron sources. Generally, a neutron reactor produces free neutrons by utilizing the chain reaction of the fission of heavy elements, such as uranium (U).^[71-72] However, the maximum neutron flux of a neutron reactor is limited by heat dissipation. The emergence of spallation neutron sources has overcome the limit of neutron flux of neutron reactors.^[73-75] As presented in Figure 2B, a spallation neutron source shares some similarities with an X-ray synchrotron source in that both accelerate particles initially in a ring. Typically, a spallation neutron source uses supply of charged heavy particles, normally hydrogen ions (H^+), which are accelerated by a linear accelerator after generation.^[76-77] The electrons are stripped off the H^+ ions, generating a medium-energy proton beam, which is further accelerated to high energy by a synchrotron ring. Subsequently, the extracted high-energy proton beam is diverted at a fixed frequency and guided to strike a cooled heavy-metal

target (e.g. tantalum (Ta) or U). When the proton beam collides with the nuclei of metal atoms, it causes spallation, breaking the metal nucleus into two or three smaller nuclei along with several neutrons. The produced neutrons are then transferred into end stations via beamlines for research, resulting in a pulsed neutron beam.

Similar to the characterization techniques developed for synchrotron radiation X-rays, various neutron-based methods have also been well established and widely applied across different field, including neutron diffraction (ND), neutron reflectometry (NR), small-angle neutron scattering (SANS), quasi-elastic neutron scattering (QENS), neutron depth profile (NDP), neutron imaging (NI), among others.^[78-81] According to the wave-particle dualism, neutrons have also a wavelength. Unlike X-rays, which interact with the electrons of matter, neutrons interact with atomic nuclei instead. Therefore, neutrons are more sensitive to light elements in the periodic table, such as hydrogen (H), lithium (Li), and their isotopes.^[79, 81-82] The high sensitivity for probing light elements makes neutron-based techniques an excellent tool for studying elemental Li within lithium batteries, allowing shorter exposure times and higher signal-to-noise ratios compared to corresponding X-ray-based measurements. While the studies using synchrotron-based X-ray methods dominate the current *in situ/operando* investigations due to their wide accessibility and versatile applications, neutron-based techniques offer unique and complementary advantages for probing ion transport and interfacial phenomena in ASSBs. A brief comparison of common neutron-based characterization techniques is also provided in **Table 2**.

Table 2. Comparison of typical neutron-based characterization techniques

Technique	Advantages	Limitations	Key insights
Neutron Diffraction (ND)	<ul style="list-style-type: none"> - Sensitive to light elements. - Probes bulk material. - Directly measures magnetic moments. 	<ul style="list-style-type: none"> - Requires large samples. - Requires crystallinity. - Low flux (long measurement times). 	Crystal structure , magnetic structure, light atom positions (e.g., H, Li), phase identification. (Å)
Neutron Reflectometry (NR)	<ul style="list-style-type: none"> - Exceptional depth resolution. - Probes buried interfaces. - Sensitive to magnetic depth profiles. 	<ul style="list-style-type: none"> - Limited to layered geometries. - Requires smooth, flat interface. - Model-dependent analysis. 	Thin film structure : thickness, density, roughness, and interdiffusion at buried interfaces. (1 - 10 nm)
Small-Angle Neutron	<ul style="list-style-type: none"> - Contrast variation via 	<ul style="list-style-type: none"> - Low flux (long count 	Nanoscale structure :

Scattering (SANS)		isotope labelling. - Probes bulk structure. - Sensitive to magnetic nanostructures.	times). - Requires contrast. - Model-dependent analysis.	particle size, shape, aggregation, pore structure. (1 - 100 nm)
Quasi-Elastic Scattering (QENS)	Neutron	- Uniquely probes atomic-scale dynamics. - Can differentiate diffusion mechanisms.	- Extremely low signal-to-noise. - Requires large samples. - Complex data analysis.	Atomic/molecular dynamics: diffusion coefficients, relaxation times. (ps - ns timescale)
Neutron Depth Profiling (NDP)		- Quantitative, non-destructive profiling. - Excellent isotopic specificity.	- Limited to specific light isotopes. - Not general elemental analysis.	Depth concentration profiles of light specific light isotopes, e.g., ^6Li , ^{10}B . (nm - μm depth resolution)
Neutron Imaging (Radiography/Tomography) NI		- High penetration through metals. - High contrast for light elements. - Non-destructive.	- Spatial resolution lower than X-ray CT. - Quantitative analysis is complex.	2D/3D density mapping, visualization of cracks, pores, fluid flow, light elements. (μm - mm)

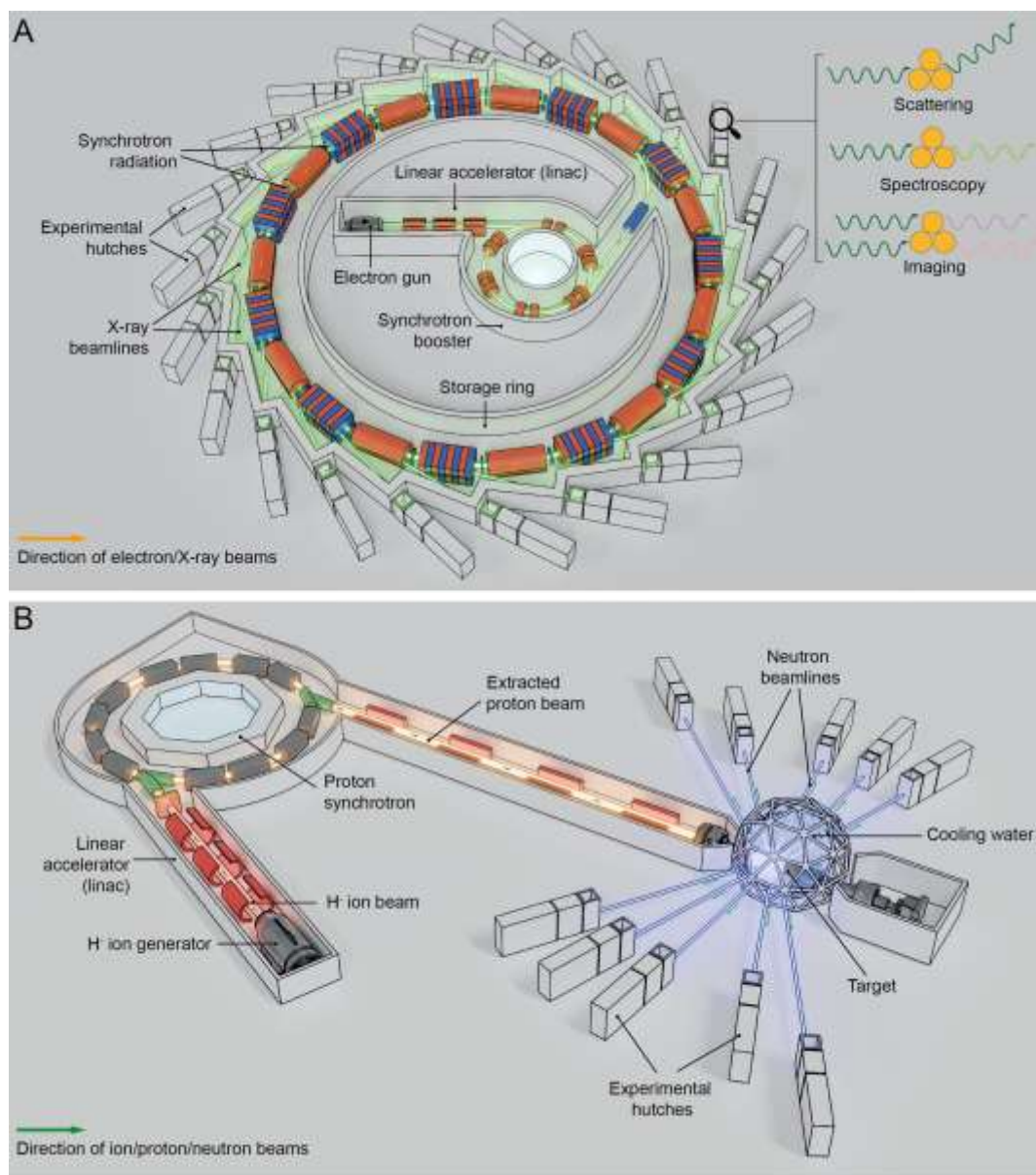


Figure 2. Illustrated schemes of simplified configurations of typical (A) synchrotron radiation source and (B) spallation neutron source. The inset located at the top right-hand corner present the three major classifications of techniques applied at synchrotron radiation light source.

Figure 3 shows major light sources (including synchrotron radiation X-ray sources and X-ray free-electron lasers) and neutron sources (including neutron reactors and spallation neutron sources) currently in operation or under construction worldwide.^[44, 83-93] Due to the high costs of construction and operation, these large scientific facilities are mainly located in the economically developed countries and regions. Synchrotron technology has now advanced to the fourth generation with extremely high brightness, which is typically 2-3 orders of magnitude greater than that of the third-generation light sources.^[83] The increase in brightness of the fourth-generation synchrotron light

ASSBs rekindled the hope for achieving this ultimate goal. Although the use of ceramic SSEs is expected to suppress the lithium dendrite growth, this issue still cannot be totally eliminated in current all-solid-state lithium metal battery (ASSLMB) systems. In addition, the physical contact and chemical stability between the lithium metal and the SSE are still non-negligible challenges. In this section, we focus on how *in situ/operando* synchrotron-based X-ray and neutron-based techniques contribute to the in-depth understanding and address these issues at the anode and anode-side interface of ASSBs.

4.1 Lithium dendrite growth

Lithium dendrite growth remains one of the most concerning issues at the anode side of ASSBs when lithium metal is employed as the anode. Although the risk of hard short circuit caused by the penetration of lithium dendrites, a serious safety risk in liquid-electrolyte lithium metal batteries, has been mitigated to a certain extent by using ceramic electrolytes in ASSBs, uncontrollable dendrite growth can still severely damage the stability of the anode interface and electrochemical performance of the battery.^[100] Therefore, understanding the growth mechanism of lithium dendrites and identifying the critical factors leading to dendrite growth are essential for realizing dendrite-free lithium metal anodes and corresponding high-performance ASSBs.

NDP is an isotope-specific and nondestructive technique for the measurement of concentration-depth distributions in the near-surface region of solids.^[101] As illustrated in **Figure 4A**, when neutrons interact with the nuclei of target element in a sample, specific nuclear reaction occurs, emitting charged particles, e.g., alpha particles and protons. As the charged particles travel through the material, they lose energy through interactions with the material's electrons. The amount of energy loss is related to the depth from which the particles originate. Finally, the emitted charged particles are collected by a detector and their energy are measured to determine the depth from which they were emitted. In particular, NDP technique is particularly well-suited for Li, Be (beryllium), B (boron), and Na (sodium) elements due to their relatively large neutron cross sections in particle-producing reactions (e. g. ${}^6\text{Li} + \text{n} \rightarrow {}^4\text{He} + {}^3\text{H}$).^[102-103] Therefore, NDP has been widely used to study lithium plating/stripping behavior and dendrite growth in ASSBs. In the study presented in Figure 4A and 4B, the NDP technique was used to operando investigate the mechanisms of lithium dendrite formation

in $\text{Li}_7\text{La}_3\text{Zr}_2\text{O}_{12}$ (LLZO), Li_3PS_4 (LPS), and LiPOH SSEs, by monitoring the dynamic evolutions of lithium concentration profiles in these SSEs.^[104] Based on the analysis of NDP and electrochemical measurements, the authors confirmed that the direct deposition of Li inside the bulk LLZO and LPS SSEs are closely related to their electronic conductivity. LLZO with higher electronic conductivity showed a higher Li content than LPS, which is lower in electronic conductivity. This study demonstrated that low electronic conductivity is a critical criterion for SSEs in their practical application in lithium metal batteries. In another study, W. Peng *et al.* used *operando* NDP to probe the nature of short-circuit and the mechanism of Li dendrite growth in garnet ($\text{Li}_{6.75}\text{La}_3\text{Zr}_{1.75}\text{Ta}_{0.25}\text{O}_{12}$)-based ASSBs.^[105] They confirmed that an electrically conductive Li-rich phase in the garnet SSE resulted in short-circuit at high current densities, which could be dynamically eliminated when the cell was under rest or operated at low current densities. The shorting caused by the Li-rich phase resembled a flash of lightning, which was triggered rapidly by the current and also quickly disappearing when the current was removed. Further analysis suggested that the formation of such short-circuit was associated with the relatively high electronic conductivity of garnet SSE ($10^{-7} - 10^{-8} \text{ S cm}^{-1}$). This finding is consistent with the study by F. Han *et al.* discussed earlier.^[104]

Complementary to NDP, NR is also a powerful tool to probe lithium dendrite growth in ASSBs, especially at interfaces. NR is a surface-sensitive technique which has already been widely used to study structures of thin films, surfaces of bulk materials, and interfaces.^[106-107] Due to the short wavelengths and sensitivity to light elements, NR has become a critical method to probe surfaces and interfaces buried in lithium-ion batteries at nanometer scale.^[108] For example, K. L. Browning *et al.* used NR to study the interfacial issue between Li anode and LiOPH SSE, as shown in Figure 4C.^[109] In Figure 4D and 4E, the obtained NR profiles, measured at the initial state, after Li plating, and after Li stripping of ASSB, were fitted by a multilayer thin film model, with each layer characterized by extracting scattering length density (SLD) and layer thickness from the fitting. SLD is a measure of the scattering power of a material, which is closely related to the chemical composition and density. This study demonstrated the formation of a Li-rich interphase layer between Li metal and LiPOH SSE after both plating and stripping. Moreover, the SLD after plating closely matched the theoretical value of Li metal, while the SLD after stripping was increased, indicating partial removal of Li during stripping, with the Li-rich layer still remaining. This residual layer suggested incomplete lithium

stripping and potential lithium dendrite growth, which could negatively impact the long-term battery performance.

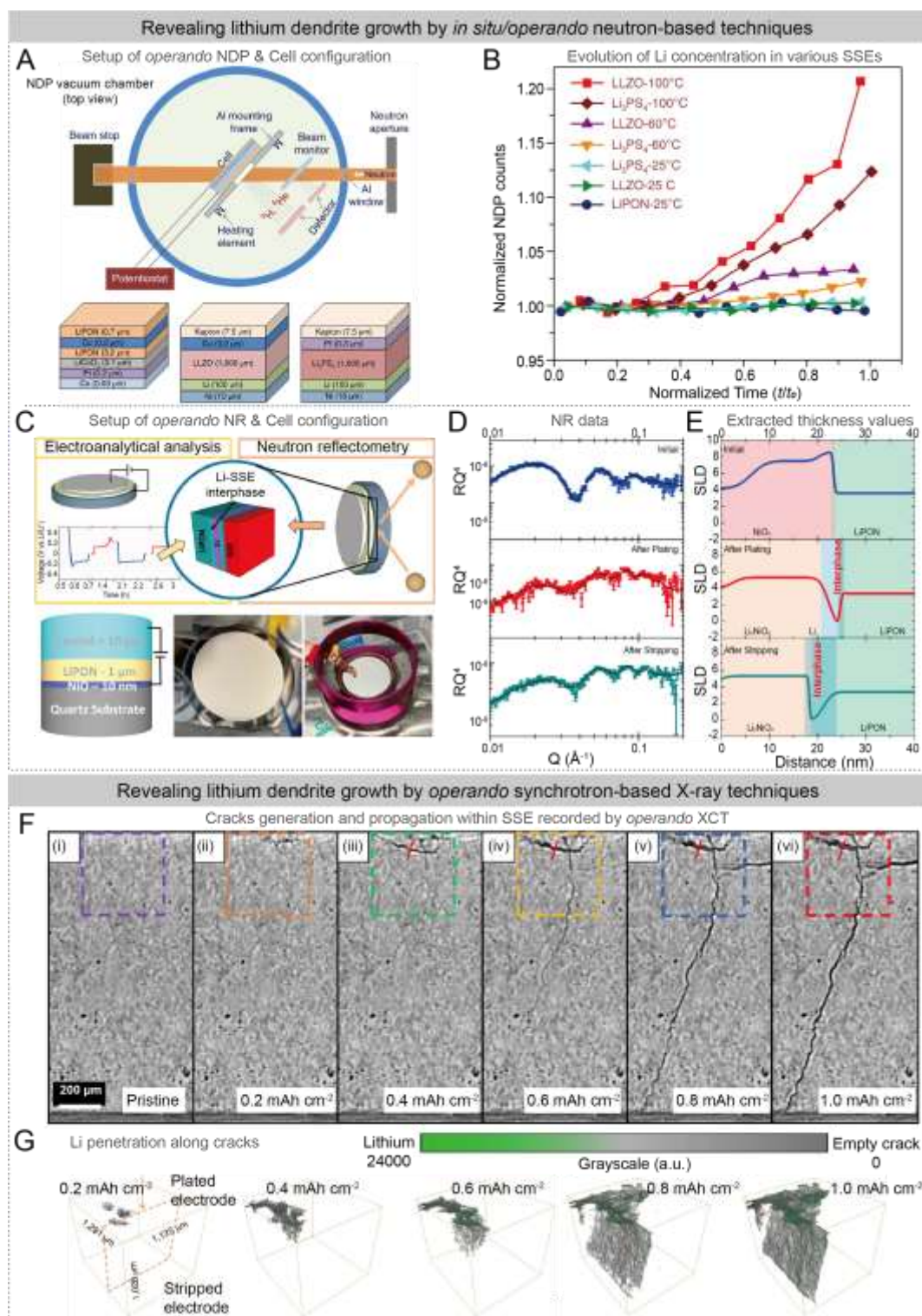


Figure 4. Selected studies on lithium dendrite growth of ASSBs by *operando* and *in situ* neutron-based and synchrotron-based X-ray techniques. (A) *Operando* NDP setup and cell structures (LiCoO₂||LiPON||Cu, Li||LLZO||Cu and Li||Li₃PS₄||Pt); (B) lithium content evolution in SSE dendrites at different temperatures. Reproduced with permission.^[104] Copyright the authors 2019,

published by Springer Nature Limited. (C) NR setup schematic and cell configuration; (D) NR data at different states; (E) corresponding SLD profiles showing modeled layer thicknesses. Reproduced with permission.^[109] Copyright 2023 American Chemical Society. (F) *In situ* phase-contrast XCT cross-sections during Li plating in a Li/Li₆PS₅Cl/Li symmetric cell; (G) 3D XCT renderings of cracks and Li deposition, highlighting crack propagation ahead of penetration. Reproduced with permission.^[110] Copyright 2021, The Author(s), under exclusive license to Springer Nature Limited.

Besides neutron-based techniques, synchrotron radiation X-rays also demonstrate its powerfulness and versatility for probing key issues at lithium metal/SSE interfaces.^[110-112] XCT, as a representative nondestructive inspection technique, has already been widely applied in medical imaging diagnosis, industrial detection, and academic research.^[113-117] XCT operates by rotating a sample under X-ray illumination and capturing a series of 2D projection images from different angles. These 2D images can be reconstructed into a 3D tomograph by computational algorithm, generating a volumetric dataset that represents the internal structure of the sample in three dimensions. Due to the high brightness and flux of X-rays generated at synchrotron sources, synchrotron-based XCT can produce 3D images within few minutes and has become an effective operando technique for probing internal structures of ASSBs.^[118] Moreover, the spatial resolution of XCT can reach sub-nanometer to nanometer level, due to the high brightness, high collimation, as well as the elaborate optical system.^[119-120] Z. Ning *et al.* presented an impressive study that employed *operando* synchrotron-based XCT to observe crack generations at the lithium anode/SSE interface, as well as crack propagation within Li₆PS₅Cl (LPSC) SSE due to the growth of lithium dendrites.^[110] As displayed in Figure 4F, an obvious transversal crack appeared after a charge of 0.4 mAh cm⁻¹ and continued to widen with increasing the current density. Meanwhile, a vertical crack formed and propagated towards the stripped (bottom) electrode the charge exceeded 0.6 mAh cm⁻². A set of 3D rendering of XCT images in Figure 4G visualized the crack propagation and lithium ingress in all directions as the current density increased, showing that both the spallation and the subsequent vertical cracks traversing the electrolyte propagated well ahead of the lithium ingress. This study provided solid evidence that generated cracks traverse the entire electrolyte before lithium reaches the other electrode and thus before the occurrence of short circuit, which is contrary to the conclusions from previous works that suggested a lithium infiltration-driven crack propagation mechanism.^{[121-}

122]

4.2 Interfacial void formation

From a general perspective, lithium dendrite growth results from a nonuniform lithium distribution during repeated stripping/plating processes, which can also induce the formation of voids or pores formed at the lithium/SSE interfaces and finally lead to a contact loss and interface deterioration.^[123-124] However, the origins of void formation and how the voids affect the interface evolution and electrochemical performance of the cells urgently needs to be investigated. The synchrotron-based XCT technique again demonstrates its powerful capabilities in this field. J. Kasmechainan *et al.* observed the accumulation of voids at the interface, as indicated by the white areas in **Figure 5A**, on the cycling of a Li/LPSC/Li cell by synchrotron-based XCT.^[125] It was confirmed that the voids generated when the stripping current removed lithium from the interface faster than it could be replenished. Based on XCT observations and related analysis, as illustrated in **Figure 5B**, the voids formation at Li/LPSC interface can be attributed to lateral lithium deposition and dendrite growth during plating. This process trapped voids within the lithium metal and eventually led to the contact loss between lithium anode and SSE. This work demonstrated the capability of XCT to recognize the voids within bulk Li and SSE. Furthermore, J. A. Lewis *et al.* employed synchrotron-based XCT to *operando* study the evolution of lithium/Li₁₀SnP₂S₁₂ (LSPS) SSE interface, aiming to uncover the intricate interactions among void formation, interphase growth, and volumetric changes that influence cell behavior.^[126] In **Figure 5C**, the set of 3D segmented renderings of the Li/LSPS interface during stripping revealed that the volume of the voids grew substantially after 3.0 mAh cm⁻² have been stripped (also seen in the zoom-in images in **Figure 5D**), which was consistent with the results of the previous study by J. Kasmechainan *et al.*^[125] Interestingly, some voids closed after plating (**Figure 5E**), while voids at the cathodic interface (**Figure 5F**) were attributed to lithium consumption caused by side reactions. Using void detection and interface analysis, the authors further investigated how the Li/LSPS contact area influenced the electrochemistry of the cell and how the volume of cell evolved during the cycling. These findings provided a comprehensive understanding of chemo-mechanical phenomena within ASSBs and demonstrated how *operando* synchrotron-based XCT accelerates the development of ASSBs.

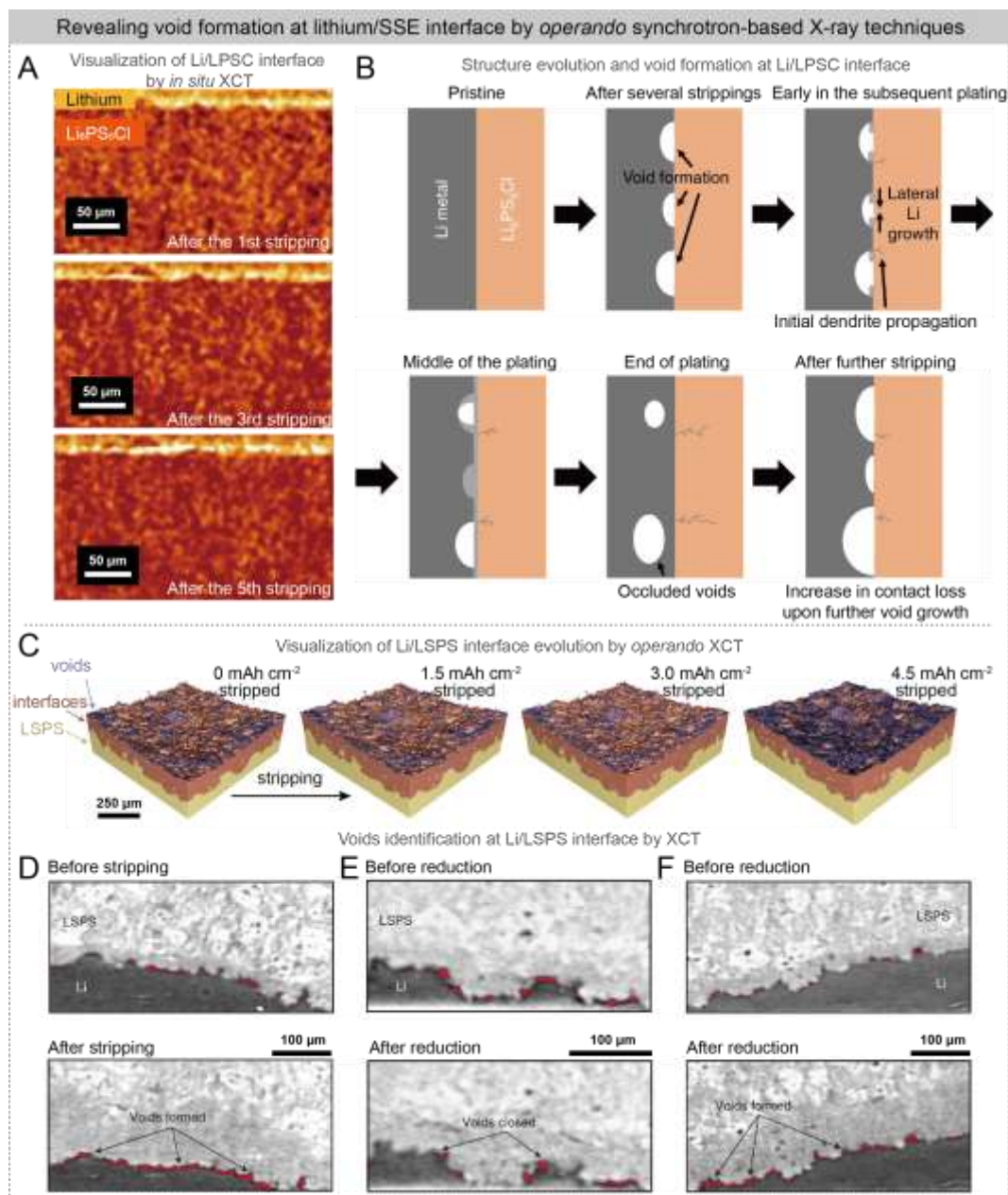


Figure 5. Selected studies on void/pore formation at the lithium/SSE interface of ASSBs by *operando* and *in situ* synchrotron-based X-ray techniques. (A) *In situ* XCT images of the Li/LPSC interface of a Li/LPSC/Li symmetric cell cycled at 1.0 mA cm^{-2} ; (B) schematic illustration of void formation and evolution at the Li/LPSC interface under current densities above the critical threshold. Reproduced with permission.^[125] Copyright The Author(s), under exclusive license to Springer Nature Limited 2019. (C) 3D renderings of the Li/LSPS interface during stripping at 1 mA cm^{-2} ; cross-sectional images of the Li/LSPS interface (D) before (top) and after (bottom) stripping at 1 mA cm^{-2} , (E) before and after reduction at 4 mA cm^{-2} , and (F) before and after reduction at 1 mA cm^{-2} , respectively. Reproduced with permission.^[126] Copyright the Author(s), under exclusive license to Springer Nature Limited 2021.

4.3 Stability of interface

Besides the issue of lithium dendrite growth, the development of ASSBs is also hindered by the incompatibility between lithium metal anode and SSE. The incompatibility usually involves the chemical reactions between lithium and SSE, potential phase transformation and structure degradation of the materials. Therefore, the characterization techniques capable of probing the atomic scale and revealing chemical environment of sample are required. XRD is one of the most widespread techniques in materials science for analyzing crystal structures, offering insights into crystallography, atomic spacing, grain orientation, strain, and defect characteristics.^[127-128] Different with XRD, which identifies scattered X-rays from crystalline matter based on Bragg's law, XAS primarily analyzes how X-rays are absorbed by an atom's core electrons. This technique is mainly employed to investigate the local chemistry, coordination, and electronic structure of materials.^[129-130] Typically, a XAS spectrum can be divided into two different regions, XANES and EXAFS, based on the absorption edge that refers to a sharp increase in X-ray absorption when the energy of the incident X-rays matches the binding energy of a core-level electron. XANES refers to the region of the X-ray absorption spectrum near the absorption edge, providing insights into the electronic structure, oxidation state, and coordination environment of the absorbing atom, whereas EXAFS refers to the region above the absorption region, giving detailed information about the local atomic structure surrounding the absorbing atom.

A comprehensive study based on multiple *in situ* and *operando* X-ray techniques was conducted by W. Li *et al*, in which Li compatibility of a vacancy-rich $\text{Li}_9\text{N}_2\text{Cl}_3$ (LNC) SSE was thoroughly investigated.^[112] This work provided an example of *in situ* dual-modal characterization for ASSBs at a synchrotron source, in which scattered X-rays and fluorescence X-rays were simultaneously collected, corresponding to XRD and XANES characterizations, respectively (**Figure 6A**). The obtained XRD patterns (**Figure 6B**) and XANES spectra (**Figure 6C-6E**) confirmed no additional crystalline phases or amorphous phases formed at the Li/LNC interface, indicating excellent thermodynamic stability between lithium and LNC SSE. Moreover, the chemical stability of the LNC SSE toward Li metal during the lithium-plating and stripping processes, was further studied by *operando* XANES measurement (**Figure 6F**). The results further confirmed the chemical stability of the Li/LNC interface during cell operation, as evidenced by the unchanged XANES spectra of the

LNC throughout the lithium plating/stripping processes. (Figure 6G-I). This series of *in situ* and *operando* studies provided a comprehensive overview of the interaction between vacancy-rich LNC SSE and Li metal under both static and operational states.

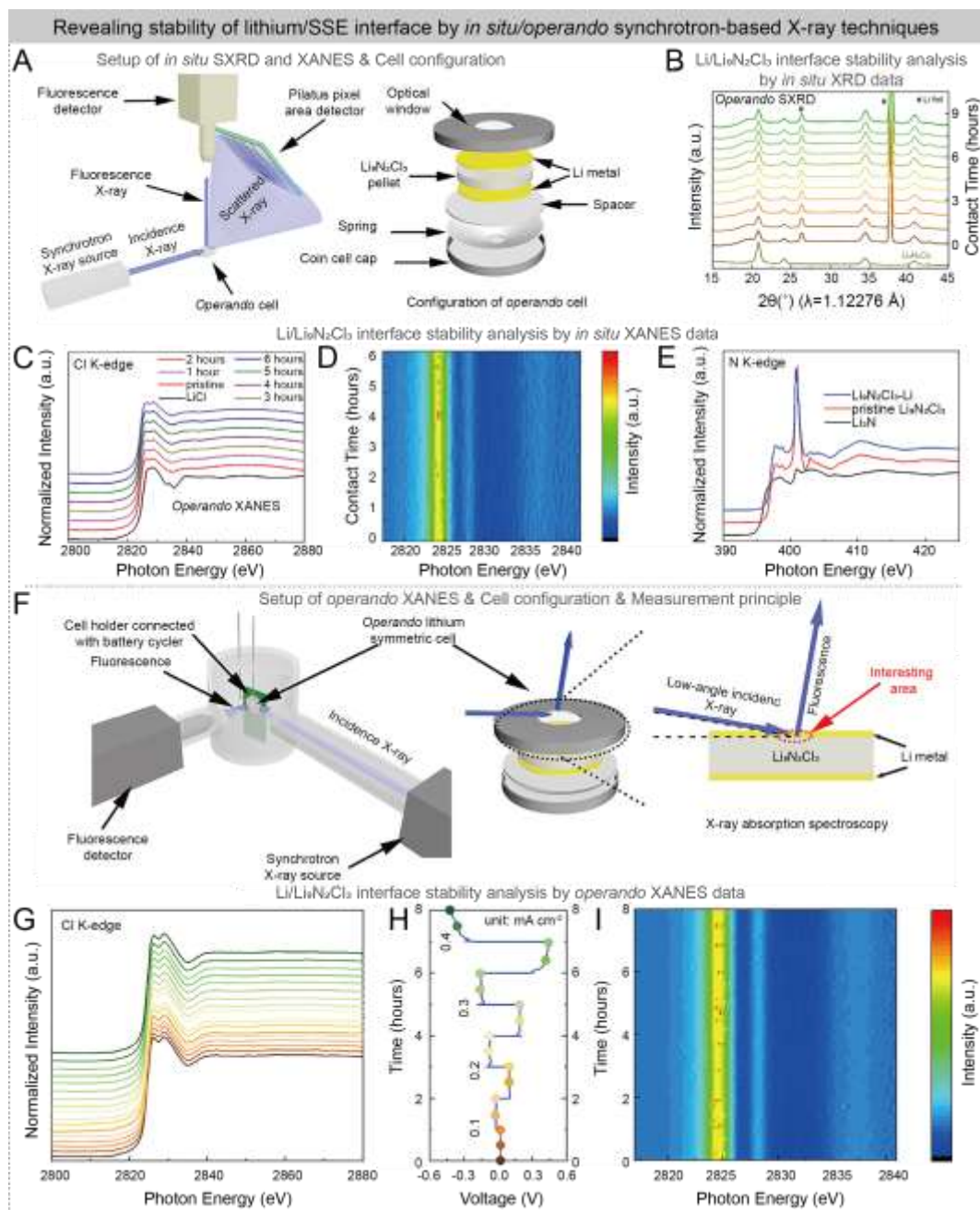


Figure 6. Selected study on the lithium anode/SSE interfaces of ASSBs by *in situ* and *operando* synchrotron-based X-ray techniques. (A) Schematic illustration of the *in situ* SXR and XANES setups; (B) *in situ* SXR pattern evolution and (C) XANES spectra at Cl K-edge with (D) first derivative mapping of the LNC SSE during contact with Li metal for several hours; (E) N K-edge XANES spectra comparison of the LNC SSE before and after contact with Li metal. (F) Schematic illustration of the *operando* XANES setups and the configuration of the *operando* cell for XANES; (G) *Operando* XANES spectra at Cl K-edge with (H) the corresponding discharge/charge voltage profiles and (I) with first derivative mapping of the LNC SSE during lithium-plating/stripping

processes. Reproduced with permission.^[112] Copyright the authors 2023, published by American Association for the Advancement of Science.

5. Probing Cathode and Cathode-Side Interface of ASSBs

The cathode side in ASSBs is more complicated than the lithium metal anode side, primarily due to the diversity of the cathode active materials and the large interfacial surface area introduced by the composite cathode architecture. This section highlights studies that mainly concentrate on four critical issues at the cathode and cathode-side interface of ASSBs as investigated using synchrotron and neutron-based techniques, including reaction mechanisms of different cathodes, interface evolution at the cathode side, the effect of the coating layer on the cathode, and thick cathode design.

5.1 Reaction mechanism of cathode

While there is broad consensus that lithium metal is the ultimate choice for anode materials of ASSBs, the most promising cathode material remains under debate. Various cathode materials that have demonstrated excellent performance in the liquid-based LIB systems are also being actively studied for their applicability in ASSBs.^[131-132] As a promising cathode candidate for ASSBs, Li_2MnO_3 (LMO) gained increasing research interests due to its high discharge capacity; however, its reaction mechanism during cycling remains sufficiently understood. K. Hikima *et al.* investigated the reaction mechanism and electronic structure changes of LMO cathode in an all-solid-state thin-film battery, using *operando* hard XPS (HAXPES) technique.^[133] XPS is a surface-sensitive analytical technique that uses X-rays to eject core-level electrons via the photoelectric effect when incident photon energy exceeds binding energy, enabling analysis of elemental composition, chemical states, and electronic structure.^[134-135] By employing hard X-rays generated at synchrotron sources, the photoelectron escape depth can reach about 30 nm, which enables the extraction of information from the bulk cathode.^[136] In this study, *operando* HAXPES spectra revealed the state evolutions of Mn and O in the LMO cathode during charge and discharge processes, as displayed in **Figure 7A** and **7B**. The results indicated that Mn and O followed different redox behaviors, corresponding to the distinct shifts in peak positions during cycling. Combined with further calculation, a reaction mechanism of LMO cathode in ASSBs was proposed: a growing number of O^{2-} gradually shift their valence to $\text{O}^{(2-a)-}$ during the initial charge of $\text{O}3\text{-Li}_2\text{MnO}_3$. Li_xMnO_3 undergoes a structural transition from O^{3-}

to O^{1-} at high voltage, while O in $O1-Li_xMnO_3$ adopts one of two distinct valences. During discharge, all O keep same valence, which gradually increases to $2-$ as the voltage decreases. The O^{1-} phase maintains stable in subsequent cycles, and the same redox trend repeating.

In response to the concern of lithium source limitation, all-solid-state sodium batteries (ASSSBs) have emerged as one of the most promising alternatives to LIBs.^[137] ASSSBs also confront challenges in selecting suitable cathode materials and optimizing electrochemical performance, where a fundamental understanding of reaction mechanism during cycling is critical to addressing these limitations. For example, B. Pandit *et al.* prepared a core-shell $Na_3V_2(PO_4)_3$ (NVP)/C composite cathode material, exhibiting good electrochemical performance in ASSSBs.^[138] To further investigate the properties of NVP/C cathode, the structural phase transitions and reaction mechanism during sodium extraction and intercalation were studied by using synchrotron-based *operando* XRD. As shown in Figure 7C, the XRD patterns revealed a first-order phase transition during the initial stage of sodium extraction in charging, forming a desodiated rhombohedral NASICON phase. Prior to full desodiation, an intermediate monoclinic $Na_2V_2(PO_4)_3$ phase emerged. Upon full charging, both $Na_3V_2(PO_4)_3$ and $Na_2V_2(PO_4)_3$ were fully converted to $NaV_2(PO_4)_3$. Although discharge reversibly restored the original phases, the intermediate $Na_2V_2(PO_4)_3$ phase was not observed in XRD patterns.

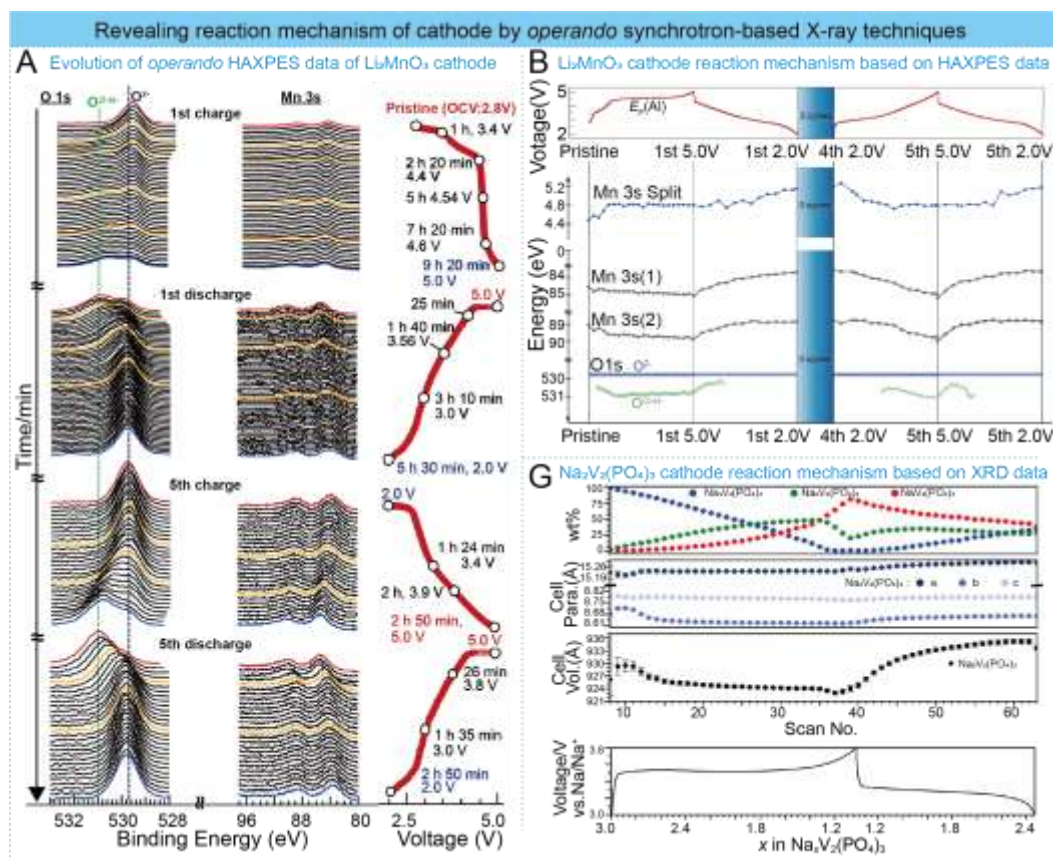


Figure 7. Selected studies on reaction mechanisms of cathodes for ASSBs by *operando* synchrotron-based X-ray techniques. (A) Summary of O 1s and Mn 3s core-level *operando* HAXPES spectra of the Li_2MnO_3 cathode in ASSB; (B) shifts in the peak positions of the Li_2MnO_3 cathode during first charge, first discharge, fifth charge, and fifth discharge. Reproduced with permission. Copyright 2021 American Chemical Society. (C) Extracted wt %, unit cell parameters, and unit cell volume of the $\text{Na}_2\text{V}_2(\text{PO}_4)_3$ phase from Rietveld refinement based on *operando* synchrotron-based XRD data. Reproduced with permission.^[138] Copyright the authors 2024, published by American Chemical Society.

5.2 Interface evolution

As previously discussed, the cathode side of an ASSB is typically a composite part consisting of cathode active material and SSE (as catholyte), which are mixed as homogenous as possible to improve overall ionic conductivity. Therefore, the cathode/SSE interface has the largest surface area among all key interfaces in ASSB and plays a major role in determining the electrochemical performance of cell. As an area of growing research interest, the issues related to the cathode/SSE interface evolution have attracted significant attention in recent years.^[139–140] A conventional view suggests that “point-to-point” ion diffusion at the interface determines the ion transport kinetics. However, by using synchrotron X-ray spectroscopic microscopy, S. Lou *et al.* provided new insights

showing that solid-solid ion transport kinetics are influenced not only by the physical interfacial contact, but also by the interior local environments within polycrystalline cathodes.^[141] An unexpected observation was initially found: an ASSB using $\text{LiNi}_{0.6}\text{Co}_{0.2}\text{Mn}_{0.1}\text{O}_2$ (NCM622) polycrystalline cathodes, poly(ethylene oxide) (PEO) SSE, and lithium metal anode exhibited the electrochemical performance at the first cycle comparable to that of a liquid-electrolyte LIB with the same electrodes. This indicated that the initial battery performance in ASSBs may not be inhibited by interfacial physical contact or the heterogeneous local environments at the interface regions.

To investigate the underlying ion transport behaviors, *operando* transmission X-ray microscopy (XTM) combined with XANES were used to obtain the Ni K-absorption edge as a function of charging time within the NCM622 cathodes of both ASSB and liquid-electrolyte LIB. XTM-XANES is an advanced dual-modal characterization technique that enables the collection of XANES spectra from 2D cross-sections within a 3D structure, exhibiting powerfulness in probing micro-scale chemical-structural relationships in materials.^[142-143] By comparing the 2D TXM-XANES mappings in **Figure 8A**, despite the different ionic transport models of “core-shell” and homogeneity, both ASSLB and LELB achieved a nearly homogenous (almost homogenous for the ASSB) charge distribution within the finally charged particles. However, the initially homogenous Li-ion transport dynamics in the ASSB cannot sustained upon cycling. As indicated in Figure 8B, the gradual failure of ion transport pathways was attributed to the continuous physical contact loss and the irreversibility of lithium transport across the interfaces. Furthermore, XCT analysis of the cycled NCM622 cathode in ASSB (Figure 8C) revealed microcracks, whose fresh exposed surfaces/interfaces-inaccessible to nonfluid solid electrolytes-aggravated phase heterogeneity, interfacial contact loss, and even the final fragmentation of polycrystalline particles. This comprehensive study based on *operando* X-ray techniques at synchrotron provided an in-depth understanding of the critical role that internal local environment within polycrystalline particles play in electrochemical reactions in ASSBs, offering key insights into underlying interfacial ion transport mechanisms. Similarly, the same team applied *operando* TXM-XANES measurement to reveal electrochemical-mechanical evolution of the $\text{FeS}_2/\text{Li}_7\text{P}_3\text{S}_{11}$ interface.^[144] They confirmed that the heterogeneous phase transformation and internal strain-induced contact loss limited electrochemical reaction in the conversion-type FeS_2 electrode.

Due to the high theoretical capacity, the FeS_2 cathode also attracted the interest of X. Sun et al.,

who applied *operando* synchrotron-based energy dispersive X-ray diffraction (EDXRD) to probe the interfacial stability between FeS₂ cathode and Li_{6.6}Ge_{0.6}Sb_{0.4}S₅I (LGSSI) SSE.^[145] Unlike XRD technique, synchrotron-based EDXRD uses polychromatic photons as the source and is usually operated at a fixed angle, which enables the rapid collection of complete diffraction patterns.^[146-147] In this study, by comparing the *operando* EDXRD results (Figure 8D and 8E) of a LGSSI/carbon||LGSSI||In-Li half-cell and a FeS₂/LGSSI/carbon||LGSSI||In-Li full-cell, respectively, it was indicated a structure degradation of the LGSSI/carbon interface while a tiny but reversible structural variation of the FeS₂/LGSSI/carbon interface. Subsequent electrochemical performance measurements showed that the FeS₂/LGSSI/carbon||LGSSI||In-Li full-cell presented a good cycling stability, confirming the dynamically stable FeS₂/LGSSI interface.

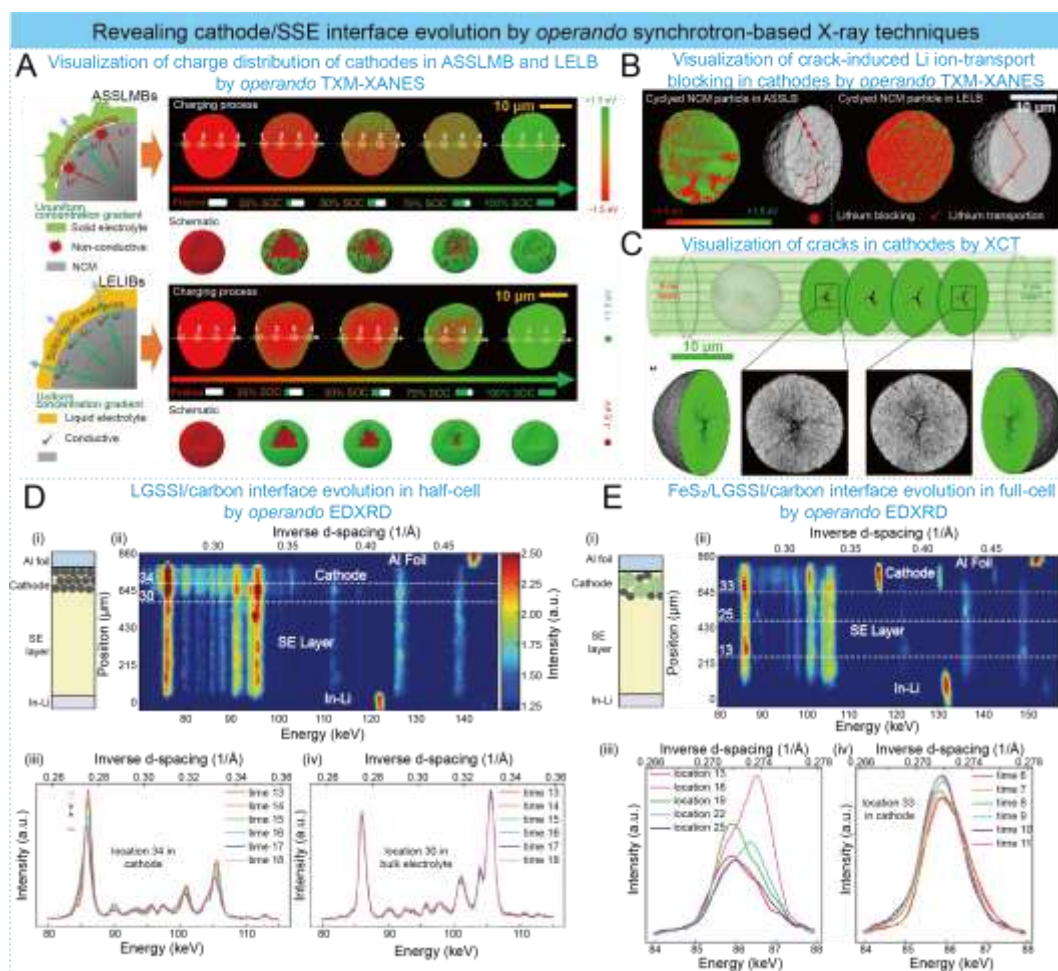


Figure 8. Selected studies on interface evolution at cathodes of ASSBs by *operando* synchrotron-based X-ray techniques. (A) *Operando* 2D TXM-XANES mapping of ASSLMBs and LELIBs during initial charging; (B) 2D TXM-XANES mapping of cycled NCM particles in ASSLBs and LELIBs, with schematic illustration of crack-induced effects on Li transport; (C) XCT images of cycled NCM622 cathode particles in ASSLBs. Reproduced with permission.^[141] Copyright the authors 2020,

published by Springer Nature Limited. (D) EDXRD results for the LGSSI/carbon||LGSSI||In-Li half-cell: (i) schematic of the half-cell; (ii) initial EDXRD mapping; (iii) major LGSSI peaks as a function of time at location 34 in the carbon cathode; (iv) major LGSSI peaks at location 30 in the SSE layer. (E) EDXRD results for the FeS₂/LGSSI/carbon||LGSSI||In-Li full-cell: (i) schematic of the full-cell; (ii) initial EDXRD mapping; (iii) variation of the LGSSI (220) peak across the pristine SSE layer at different locations; (iv) LGSSI (220) peak at location 33 inside the FeS₂ cathode as a function of time. Reproduced with permission.^[145] Copyright 2020 Wiley-VCH GmbH.

5.3 Effect of coating layer

Previous studies have shown that many cathode/SSE pairs are thermodynamically unstable, especially for the combinations of NCM cathodes and sulfide-based SSEs. However, the high theoretical capacity of the NCM cathode materials and the high ionic conductivity of sulfide-based SSEs are highly attractive for the pursuit of high-performance ASSBs. Recently, coating NCM cathodes with various materials, such as Li₂S-P₂S₅, Al₂O₃, LiNbO₃, and LiPO₄, have been demonstrated as an effective strategy to improve the electrochemical performance of sulfide-based ASSBs.^[148-152] However, the reaction mechanisms and structural evolution at coated-cathode/sulfide SSE interfaces and how the coating layer protects the cathode remain inadequately understood.

To understand the role of coating layer on stabilizing the cathode-side interface and enhancing electrochemical performance, X. Li *et al.* applied *operando* XANES, combined with other characterizations, to investigate the interface evolution at Li₁₀GeP₂S₁₂(LGPS) SSE and LiNi_{0.8}Mn_{0.1}Co_{0.1}O₂ (NCM811) cathode with and without LiNbO_x (LNO) coating.^[55] A 5 nm-thick LiNbO₃ (LNO) layer was uniformly coated on NCM811 particles via atomic layer deposition (ALD). The analysis of S K-edge spectra (**Figure 9A-B**) revealed LGPS SSE decomposition in bare NCM811-LGPS cells (as evidenced by the peak shifts around 2470 eV – 2471 eV during cycling), whereas LNO-coated cathodes showed good stability indicated by the unchanged peak in the spectra. Both systems exhibited similar trends in Ni K-edge evolution, while Mn/Co K-edge spectra revealed the inherent instability of Mn during delithiation/lithiation. In the bare cathode, interfacial parasitic reactions led to structural degradation and impurity formation, reducing ionic conductivity, whereas the LNO layer blocked sulfur diffusion, stabilized the cathode-electrolyte interface and improved ASSB performance.

X. Liu *et al.* also adopted the same strategy that coating LNO layer on single-crystal NMC811 (S-NMC811) cathode to enhance the interface stability when paired with LSPS SSE.^[153] Instead of

comparing the cathode/SSE interface stability with and without LNO coating, the authors in this study specifically focused on probing how the coating layer improves the interface stability and improves electrochemical performance. *Operando* XRD results of bare S-NCM811/LSPS ASSBs (Figure 9C) revealed the growth of a sluggish phase during cycling when charging the cell to 4.35 V, correlating with capacity fade. A more focused analysis of the peak evolution (Figure 9D) indicated that the sluggish phase persisted even at ultralow currents (<0.001 mA), attributed to interfacial side reactions proportional to NCM/LSPS contact area, which promoted thick cathode electrolyte interface (CEI) formation and surface reconstruction. Coating S-NCM811 with LNO suppressed these reactions, as indicated by the XRD patterns in Figure 9E, drastically reducing the sluggish phase and enhancing cell performance. These two studies are complementary on revealing the significant role to suppress interfacial side reactions and stabilize the interfacial structure from both chemical and physical perspectives.

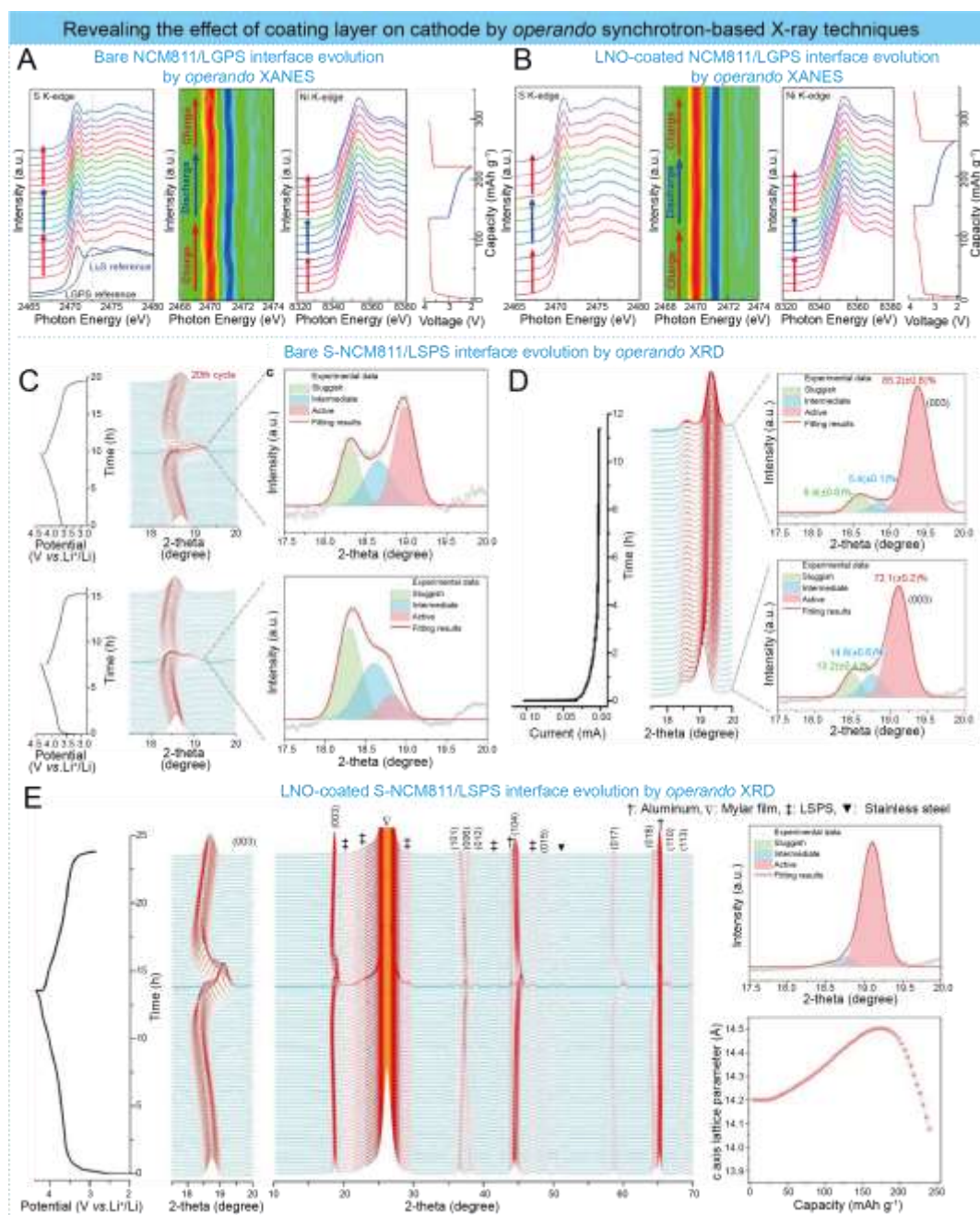


Figure 9. Selected studies on the coating layer for the stabilized cathode/SSE interfaces of ASSBs by *operando* synchrotron-based X-ray techniques. *Operando* S K-edge spectra with first derivative mapping, Ni K-edge spectra, and charge/discharge profiles of (A) bare NCM811/LGPS and (B) LNO-coated NCM811/LGPS ASSBs. Reproduced with permission.^[55] Copyright 2019 American Chemical Society. (C) The evolution of (003) peak of S-NCM811 cathode extracted from *operando* XRD patterns in different cycles and corresponding analysis; (D) the evolution of (003) peak of S-NCM811 cathode extracted from *operando* XRD patterns and corresponding analysis; (E) *Operando* XRD patterns and corresponding analysis of LNO-coated S-NCM811/LSPS ASSB during initial charge/discharge process. Reproduced with permission.^[153] Copyright 2022 Elsevier B.V.

5.3 Thick cathode design

To achieve ideal high-energy ASSBs, a thick or high-loading cathode (ideal thickness of 45 – 200 μm) is both an essential component and a key challenge in engineering.^[154-155] When increasing the thickness of the cathode, typically composited with CAM and SSE, the transport behavior of lithium ions within the thick electrode may differ significantly from that in a thin electrode. In regard to this issue, A. M. Stavola *et al.* revealed the electrochemical nonuniformity and tortuosity factors within cathodes as a function of CAM fraction in the NCM111/LPSC composite cathode (110 μm in thickness) by using *operando* EDXRD measurements.^[156] **Figure 10A** showed *operando* EDXRD data of the all-solid-state (ASS) cells with different cathode architectures (as sketched in Figure 10B) during the initial two cycles, in which color mapping represented spatially resolved Li content ($1 - x$) in lithiation across the cathode thickness. The results clearly showed that the 70 % and 40 % CAM cells exhibited preferential delithiation near the current collector side during charge 1, while the trend was reversed in the 80 % CAM cell. This phenomenon was attributed to the effect of the tortuosity factor in the cathode. Applying a $\text{Li}_{0.35}\text{La}_{0.5}\text{Sr}_{0.05}\text{TiO}_3$ coating did not change the nature of the lithiation gradient during charge 1 but did smooth the current distribution subsequently. Lithiation gradients on a larger scale were displayed in Figure 10C. The 70 % CAM cells showed the smallest gradients of a maximum Δx of 0.145 without the coating and 0.209 with the coating. Figure 10D provided the total electrochemical reactions for each cathode slide for each cycling stage. The 70 % CAM cells presented more uniform distribution of the reactions across the cathode compared to other two cells. Therefore, loading of 70 % CAM should be the optimized composition of the cathode. Deviations from this optimal loading resulted in more pronounced gradients.

Based on these *operando* EDXRD and further simulation results, the authors suggested that the observed lithiation gradient (current distribution) in sulfide-based composited cathodes should be a key consideration for practical design of ASSBs with a thick cathode. In a preprint study, the authors designed a three-layer composite cathode in which each layer had a different ratio of CAM and SSE, achieving a mass-loading of 33 mg cm^{-2} (180 μm).^[157] It was proposed that this architecture can promote fast lithium-ion transport and uniform reaction throughout the entire thick cathode, ultimately leading to enhanced electrochemical performance.

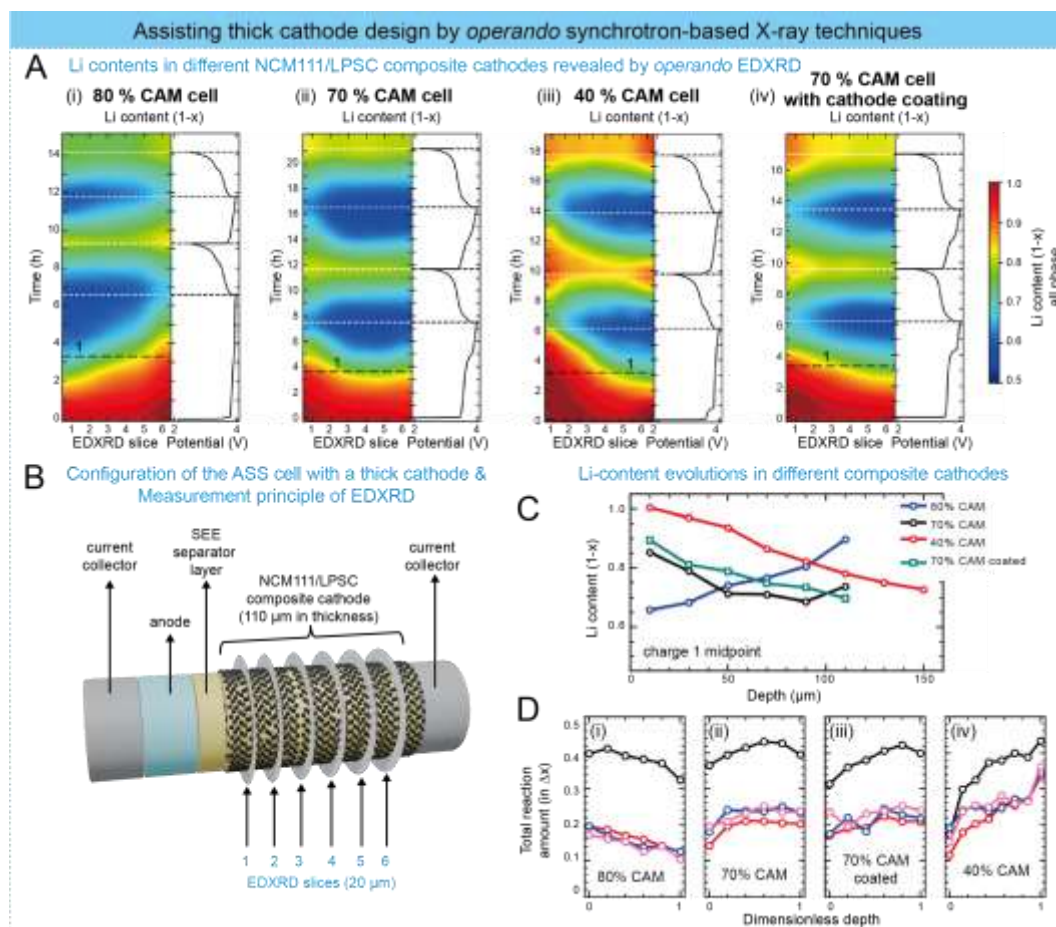


Figure 10. Selected study on the thick cathode design of ASSBs assisted by *operando* synchrotron-based X-ray techniques. (A) *Operando* EDXRD data for initial cycling of NMC111/LPSC cathodes as a function of cathode composition; (B) the concept of the ASS cell with a thick 110 μm cathode, with EDXRD data taken in six 20 μm slices to observe nonuniformity through the cathode thickness; (C) lithiation profiles for each cell at the midpoint of charge 1, which are marked by note 1 and black dash lines in Figure 10A; (D) Spatially resolved total reaction amounts in Δx during each cycling stage for different cathode compositions. Reproduced with permission.^[156] Copyright 2023 American Chemical Society.

6. Probing SSE and SSE/SSE Interface of ASSBs

As the most important component of ASSBs, the SSE receives significant attention for its stability, structural evolution, and degradation mechanism. The related studies using in situ/*operando* X-ray and neutron measurement will be discussed in this section. As the SSE is the interlayer between anode and cathode, investigations into these critical issues of the SSE naturally involve the anode/SSE or cathode/SSE interfaces. Therefore, this section serves as a supplementary of the previous two sections. In addition, with the fast development of ASSBs in recent years, emerging issues related the

SSE/SSE interface will also be introduced.

6.1 Stability and structural evolution of SSE

Due to high ionic conductivity and good compatibility with cathode materials, halide-based SSEs are regarded as one of the most promising SSEs to realize a commercial application in ASSBs. However, air stability remains a major concern of halide-based SSEs, requiring both improvement and a deeper understanding of the underlying degradation mechanisms. W. Li *et al.* for the first time, applied *in situ* SXRD and *in situ* XANES to investigate the air stability of Li_3InCl_6 (LIC) SSE.^[158]

As illustrated in **Figure 11A**, the LIC sample was exposed to air with 30% relative humidity under the *in situ* SXRD characterization. As shown by the evolution of SXRD patterns in Figure 11B, a significant change occurred after 10 min exposure to air, indicating the formation of $\text{Li}_3\text{InCl}_6 \cdot x\text{H}_2\text{O}$. In addition, the intensity of the two new peaks belonging to LiCl gradually increased with the exposure time. To determine which components of air were responsible for the reactions with Li_3InCl_6 , *in situ* XANES measurements were carried out when the Li_3InCl_6 sample was exposed to dry air and moisture, respectively, as illustrated in Figure 11C. According to the XANES spectra in Figure 11D-11F, it can be concluded that moisture is the primary reason of LIC degradation, leading to the loss of ionic conductivity.

Another pioneering work was reported by Y. Liang *et al.*, in which *operando* grazing-incidence wide-/small-angle X-ray scattering (GIWAXS/GISAXS) techniques were employed to study the crystalline structure and morphology evolutions of polymer electrolyte in ASSBs.^[159] As the name suggests, GIWAXS/GISAXS are specific modes of WAXS/SAXS with very small incident angles of the X-ray radiation with respect to the sample surface (normally $< 1^\circ$), enabling the extraction of valuable information from a larger area due to the large footprint on the buried morphology, structure, and orientation of the bulk films.^[160-161] Due to the difference of the sample-to-detector distance (SDD) in GIWAXS and GISAXS setups, simultaneous measurements using both techniques are possible, as shown in Figure 11G. In this work, an ASSB using PEO-based composite electrolyte (PCE) was fabricated. The evolution of the crystal structure of the PCE was analyzed by *operando* GIWAXS data, as presented in Figure 11H. At the first glance, a distinct peak evolution appeared at around $q = 1.6 \text{ \AA}^{-1}$, which was attributed to the reduction process of the PEO- Li^+ group at 1.57 V, where the coordination bond unfolded to release free Li^+ for further deposition. Further in-depth analysis

provided the evolutions of the PEO and LiTFSI sub-peaks, which collectively suggested the presence of a more amorphous phase within the PCE, facilitating the Li^+ transport process. Simultaneously, the buried morphology evolutions of the PCE were detected by *operando* GISAXS measurements, as shown in Figure 11I. Through detailed analysis by modeling the line cuts of the 2D GISAXS data, it was found that the PEO-LiTFSI domain radius and the center-to-center distance increased during the PEO reduction process, corresponding to the intensity decrease of the PEO- Li^+ coordination peak. Moreover, the increase in the PEO-LiTFSI domain radius and distance was found at 1.15 V, whereas the decreased intensity of the LiTFSI Bragg peak were observed as a result of the TFSI-decomposition reaction and SEI formation. During the Li^+ plating and stripping processes, only the PEO-LiTFSI domain radius changed due to ion transport. An increase in domain radius during the irreversible electrochemical reaction promotes the expansion of the amorphous phase, thereby enhancing ionic conductivity. In contrast, the decrease in radius observed during Li^+ plating and stripping reveals the Li^+ transport mechanism through the polymer chain.

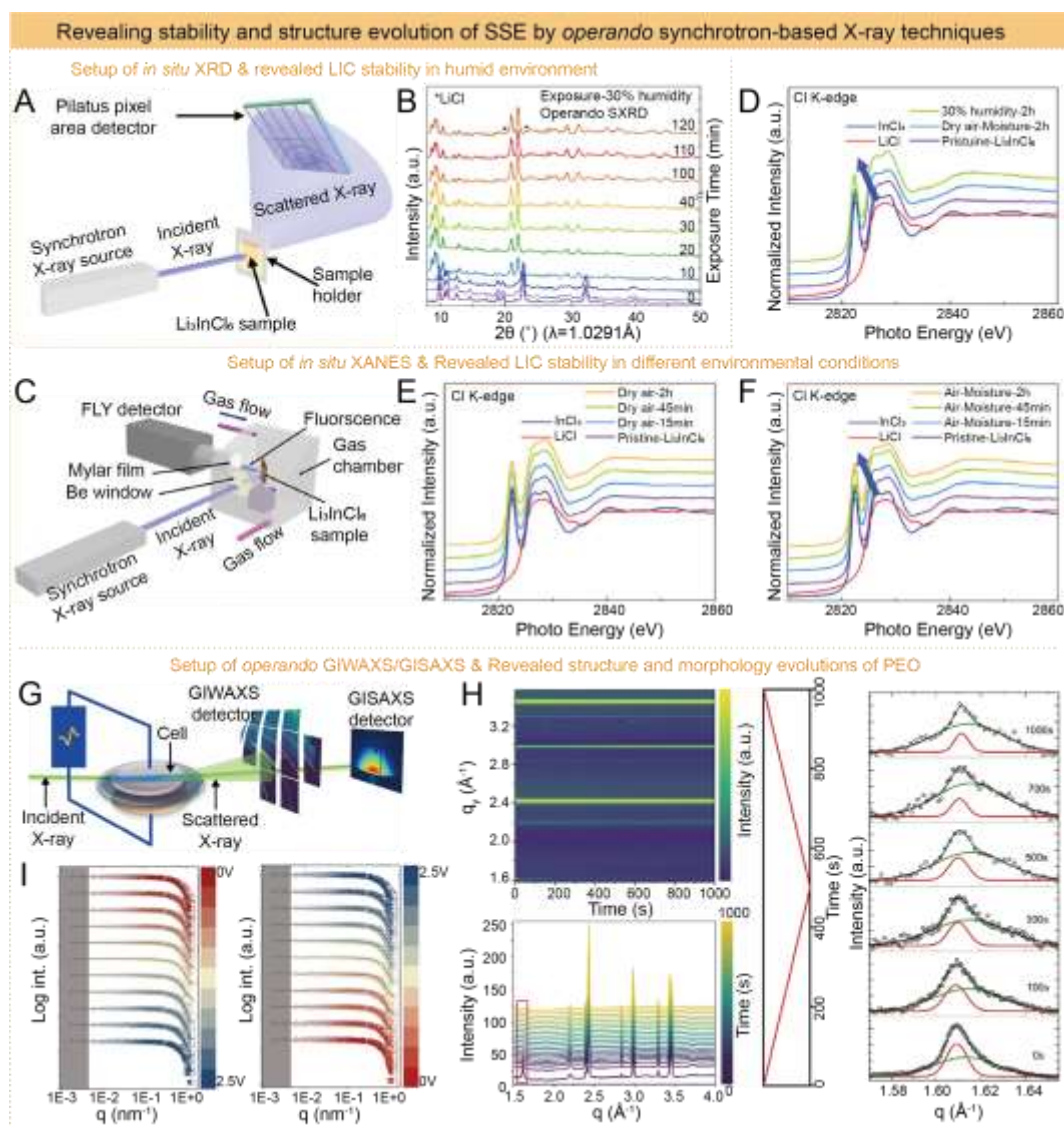


Figure 11. Selected studies on the SSEs of ASSBs by *operando* and *in situ* synchrotron-based X-ray techniques. (A) Schematic of *in situ* synchrotron XRD on Li_3InCl_6 SSE exposed to 30% humidity; (B) corresponding XRD patterns over time. (C) Schematic of *in situ* synchrotron XANES on Li_3InCl_6 SSE under different gas environments, with Cl K-edge XANES spectra during exposure to (D) dry air and moisture, (E) dry air, and (F) Ar and moisture (120 min). Reproduced with permission.^[158] Copyright 2020 American Chemical Society. (G) Schematic of *operando* study of Li||PEO composite electrolyte||Cu cell using simultaneous synchrotron-based GISAXS and GIWAXS, with corresponding (H) GIWAXS and (I) GISAXS results. Reproduced with permission.^[159] Copyright the authors 2024, published by American Chemical Society.

6.2 Degradation mechanism of SSE

Due to the brittleness of pressed ceramic SSE pellets, they always suffer from structural degradation by chemical and mechanical factors during cycling processes not only at the interfaces closed to cathodes/anodes but also in the bulk.^[162-163] Therefore, in-depth understanding the degradation mechanism of bulk SSEs a prerequisite for the development of high-performance SSEs.

J. Tippens *et al.* used *in situ* XCT to visualize fracture processes and interphase growth in a NASICON-type $\text{Li}_{1+x}\text{Al}_x\text{Ge}_{2-x}(\text{PO}_4)_3$ (LAGP) SSE during cycling of a Li/LAGP/Li symmetrical cell, establishing a correlation between mechanical degradation and electrochemical behavior.^[164] **Figure 12(A)** and **12(B)** provided the structural evolution of LAGP SSE revealed by *in situ* XCT measurements before and during cycling with different time. A progressive increase in crack formation within the LAGP pellet was clearly observed during cycling. After 24 hours of cycling, isolated radial cracks formed, which lengthened and thickened with continued cycling. This was followed by the development of circumferential cracks and interconnected crack networks linked to the radial features. Further *in situ* measurement showed a strong correlation between the crack propagation and electrochemical impedance, as shown in **Figure 12(C)**, indicating that electrochemical failure of these cells was caused by the mechanical fracture. Moreover, the XCT scans along the cross-section of LAGP SSE, as presented in **Figure 12 (D)**, suggested that the cracks initiated near the edge of the lithium/LAGP contact area, with some of the thickest visible cracks propagating from this region. This finding indicated that the structural degradation of LAGP SSE was strongly influenced by the LAGP/Li interface.

Another strong example for applying *in situ* XCT to reveal degradation behavior of SSE was presented by M. B. Dixit *et al.*, who conducted an in-depth investigation into how solid electrolyte microstructure and interfacial decomposition affect failure mechanisms of LPS SSE.^[165] The authors prepared a series of LPS SSEs with various microstructure and interphase properties: amorphous LPS (A-LPS), a mixture of A-LPS and LiI (LPS:0.5LiI), a mixture of A-LPS and LiI after mechanical milling (LiI-AT), and a mixture of A-LPS and LiI after mechanical milling and further annealing (LiI-AN). In **Figure 12E**, the 3D rendering extracted from *in situ* XCT images of different Li/SSE/Li cells cycled to failure, highlighting the onset and progression of mechanical failure (cracks). The charge-to-failure values of these cells followed the trend $\text{A-LPS} < \text{LPS:0.5LiI} < \text{LiIAT} < \text{LiI-AN}$ (around 25, 35, 40, and 90 mC, respectively). Visibly, the cracks within the A-LPS, LPS:0.5LiI, and LiI-AT SSEs were mainly localized in a specific region, while the cracks were uniformly distributed in the LiI-AN cell. When focusing on the crack propagation in one SSE during cycling, an example of the LiI-AN sample shown in **Figure 12(E-v)**, it was found that all these SSE materials followed two distinct failure modes: (1) edge-chipping failure at the Li/SSE interface and (2) vertical crack growth through

sample thickness originating from the edge-chip. This study also demonstrated that the failure of SSE by cracks growth was highly related to the evolution and contact loss (void formation) of the electrode/electrolyte interface. Both two studies highlight that the origin of SSE structural degradation has a close relevance to the properties of electrode/SSE interface, such as contact loss and interphase formation.

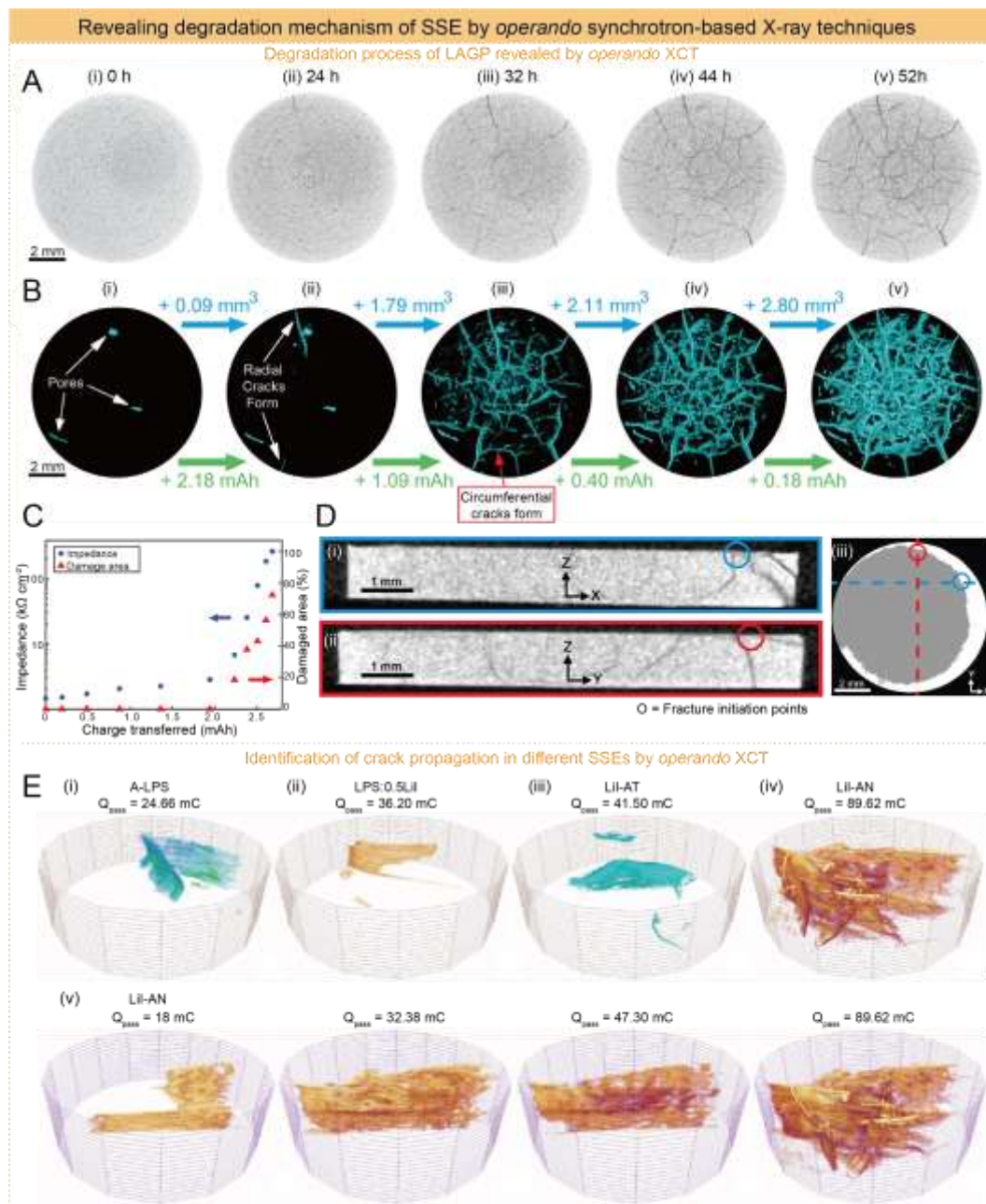


Figure 12. Selected studies on degradation mechanisms of SSEs in ASSBs by *operando* synchrotron-based X-ray techniques. (A) 2D slices from the center of a LAGP pellet extracted from 3D tomograms (i) before cycling and (ii-v) after various cycling times; (B) 3D crack networks throughout the pellet at corresponding time points; (C) impedance evolution of a separate cell as a function of total charge transfer; (D) cross-sectional XCT slices in different orientations after cycling. Reproduced with permission.^[164] Copyright 2019 American Chemical Society. (E) 3D crack structures of cycled

samples: (i) A-LPS, (ii) LPS:0.5LiI, (iii) LiI-AT, and (iv) LiI-AN, with (v) crack propagation in LiI-AN during plating/stripping. Reproduced with permission.^[165] Copyright 2020 Elsevier Inc.

6.3 Crack propagation at SSE/SSE interface

In recent years, multi-layer-SSE configurations in ASSBs gained increasing attention as they can avoid severe drawbacks of single-layer-SSE ASSBs. For example, pairing a halide-based SSE with a cathode and pairing a sulfide-based SSE with a Li metal anode can effectively enhance the cycling stability of ASSBs, as this strategy leverages the respective strengths of halide-based SSEs (good stability with cathode materials) and sulfide-based SSEs (good compatibility with lithium metal).^[166-167] In contrast to create more stable interfaces, instable interfaces surprisingly present positive effects on the performance of ASSBs in certain cases. L. Ye *et al.* designed a multi-layer SSE structure of a less-stable electrolyte sandwiched between two more-stable solid electrolytes ($\text{Li}_{5.5}\text{PS}_{4.5}\text{Cl}_{1.5}||\text{LGPS}||\text{Li}_{5.5}\text{PS}_{4.5}\text{Cl}_{1.5}$). This structure prevented Li dendrite growth through well localized decompositions in the less stable electrolyte layer by a mechanism involving chemical reaction between the lithium metal dendrite and the inner layer material, which blocked crack propagation via an “expansion screw” effect.^[168]

In this configuration, the less stable inner layer plays a key role for inhibiting Li dendrite growth. Therefore B. Hu *et al.* investigated different crack deflection mechanisms of the multi-layer-SSE architectures with different inner layers by using *operando* X-ray CT imaging.^[169] The cells were constructed with LPSC SSE as symmetrical outer layers, Li_3ScCl_6 (LSC), LGPS, and LPS as inner layers, sandwiched between lithium metal electrodes and operated under the same stack pressure. As presented in **Figure 13A-13C**, in the $\text{LPSC}||\text{LSC}||\text{LPSC}$ cell, spallation cracks generated at the LPSC-top Li interface, propagated vertically through the LPSC layer, then deflected at the LPSC-LSC interface and further spread within the inner layer, rather than continuing directly toward the bottom Li electrode. The cell finally survived under a current density of at least 15.25 mA cm^{-2} without short-circuit. In the LPSC/LGPS/LPSC cell, crack propagation followed a similar behavior to the LSC inner layer, with cracks forming at the top of LGPS, reaching the LGPS-LSC interface, and deflecting into the inner LGPS layer (Figure 13D, 13E). However, unlike the previous LSC case, the cracks were unexpectedly filled after reaching the interface between LGPS and upper LPSC layer. It was confirmed that Li metals reached the regions of the dry crack just formed in the inner layer, reacted

with the LGPS, and formed reaction products that filled the cracks. By this way, the Li dendrite propagation was effectively inhibited and the LPSC||LGPS||LPSC cell can be plated at a current density of at least 16.75 mA cm^{-2} without short-circuit, as shown in Figure 13F. The LPSC||LPS||LPSC cell exhibited the worst result in this comparison, in which a transverse crack passed through all the SSE layers without deflection or refilling, resulting in a quick short-circuit at 2.75 mA cm^{-2} (Figure 13G-13I). The authors further discussed the origins of crack deflection along the SSE interfaces. They concluded that the crack deflection at the SSE interface is determined by mechanical rather than chemical properties of the SSE layers, which involves the Young's moduli of each layer, normal and shear strains at the interfaces, and surface roughness. This study offered a new perspective on multi-layer SSE design beyond just considering ionic conductivity and chemical compatibility of SSEs.

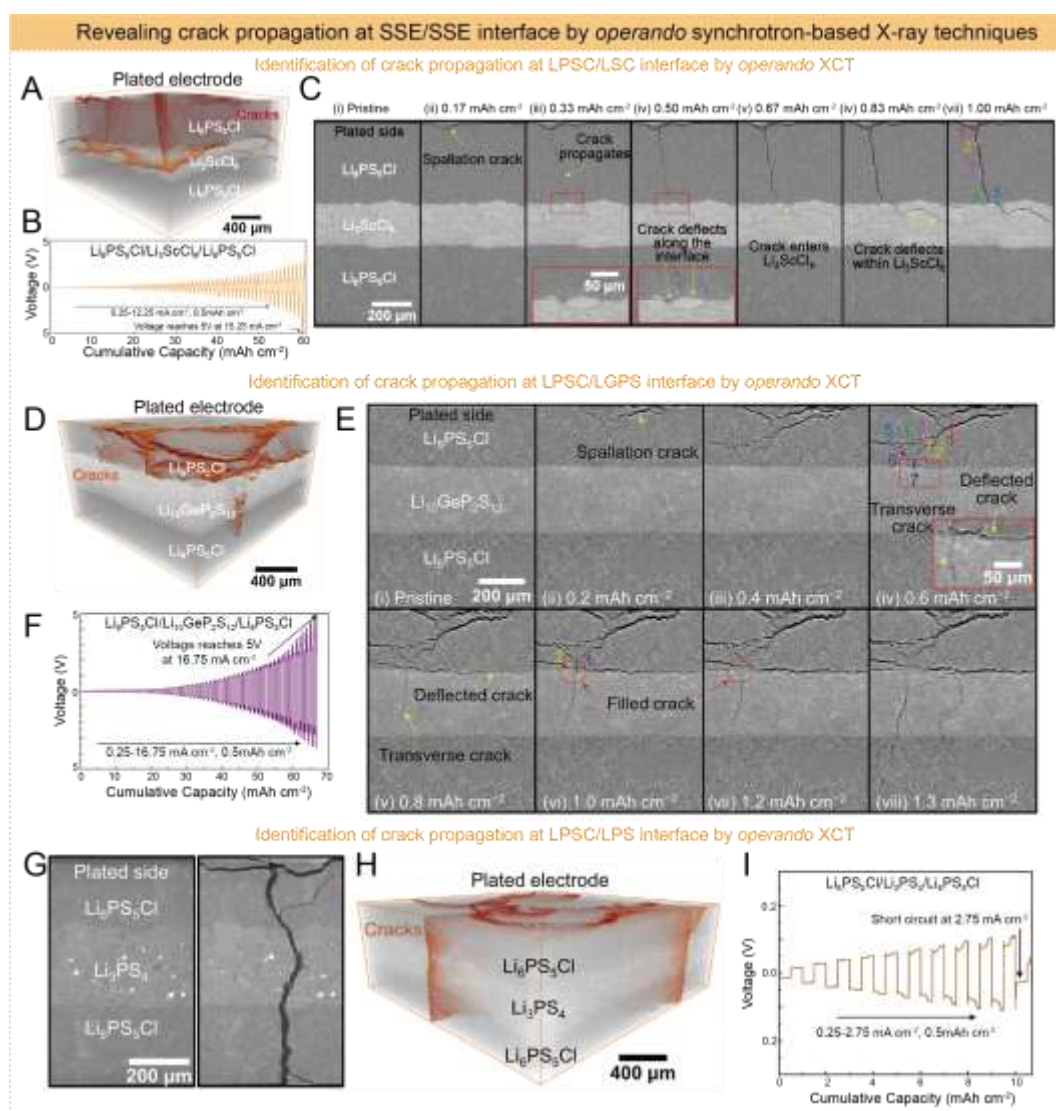


Figure 13. Selected study on the SSE/SSE interfaces of ASSBs by operando synchrotron-based X-ray techniques. (A-C) Electrochemical data and XCT virtual cross-sections from the

Li/Li₆PS₅Cl/Li₃ScCl₆/ Li₆PS₅Cl/Li cell; (D-E) electrochemical data and XCT virtual cross-sections from the Li/Li₆PS₅Cl/Li₁₀GeP₂S₁₂/Li₆PS₅Cl/Li cell; (G-I) electrochemical data and XCT virtual cross-sections from the Li/Li₆PS₅Cl/Li₃PS₄/Li₆PS₅Cl/Li cell. Reproduced with permission. Copyright the authors 2024. Published by Elsevier Inc.^[168]

7. Probing Cell-Level Issues of ASSBs

Besides the specific studies focusing on individual components or interfaces within ASSBs, an increasing number of investigations are addressing cell-level issues, fully leveraging the advantages of *in situ/operando* synchrotron-based X-ray and neutron-based techniques for large-scale probing. In this section, we review how scientists have used these advanced techniques to reveal the transport of lithium ions, electro-chemo-mechanical coupling issues, and safety issues of ASSBs at synchrotron and neutron sources.

7.1 Lithium-ion transport

Li-ion transport and distribution within a battery directly impact the performance and quality of ASSBs, including energy density, charging time, and operation safety. Due to high sensitivity to light elements, neutron-based methods enable real-time tracking of the transport of lithium ions in operated ASSBs. T. Kobayashi *et al.* demonstrated a near real-time quantitative lithium-tracking method by utilizing a high-intensity thermal neutron source and lithium-6 as a tracer in a thermal neutron-induced nuclear reaction (i.e. NDP measurement as introduced previously).^[170] A Pt||LiCoO₂||Li₃PO₄||Ta cell with a lithium-6-enriched positive electrode was prepared as the sample for tracking lithium ions during the charging process. **Figure 14A-14C** present the energy spectra obtained from the battery before, during, and after charging at various spectrum acquisition times. The evolutions of peak features in the spectra were not obvious for further analysis until the acquisition time was increased to 1 hour, as shown in Figure 14C. Based on the analysis of obtained energy spectra and the results of simulation, a vacancy migration mechanism for lithium-ion transport was proposed by the authors. As illustrated in Figure 14D, a lithium ion from the solid electrolyte on the negative electrode side migrates into the negative electrode, which generated a vacancy in the solid electrolyte on that side. Subsequently, another lithium ion migrated in to fill this vacancy, causing the vacancy to shift progressively towards the solid electrolyte on the positive electrode side. Eventually, a lithium ion from the positive electrode fills the vacancy. In this process, the lithium ions

in the solid electrolyte were gradually replaced by those from the positive electrode.

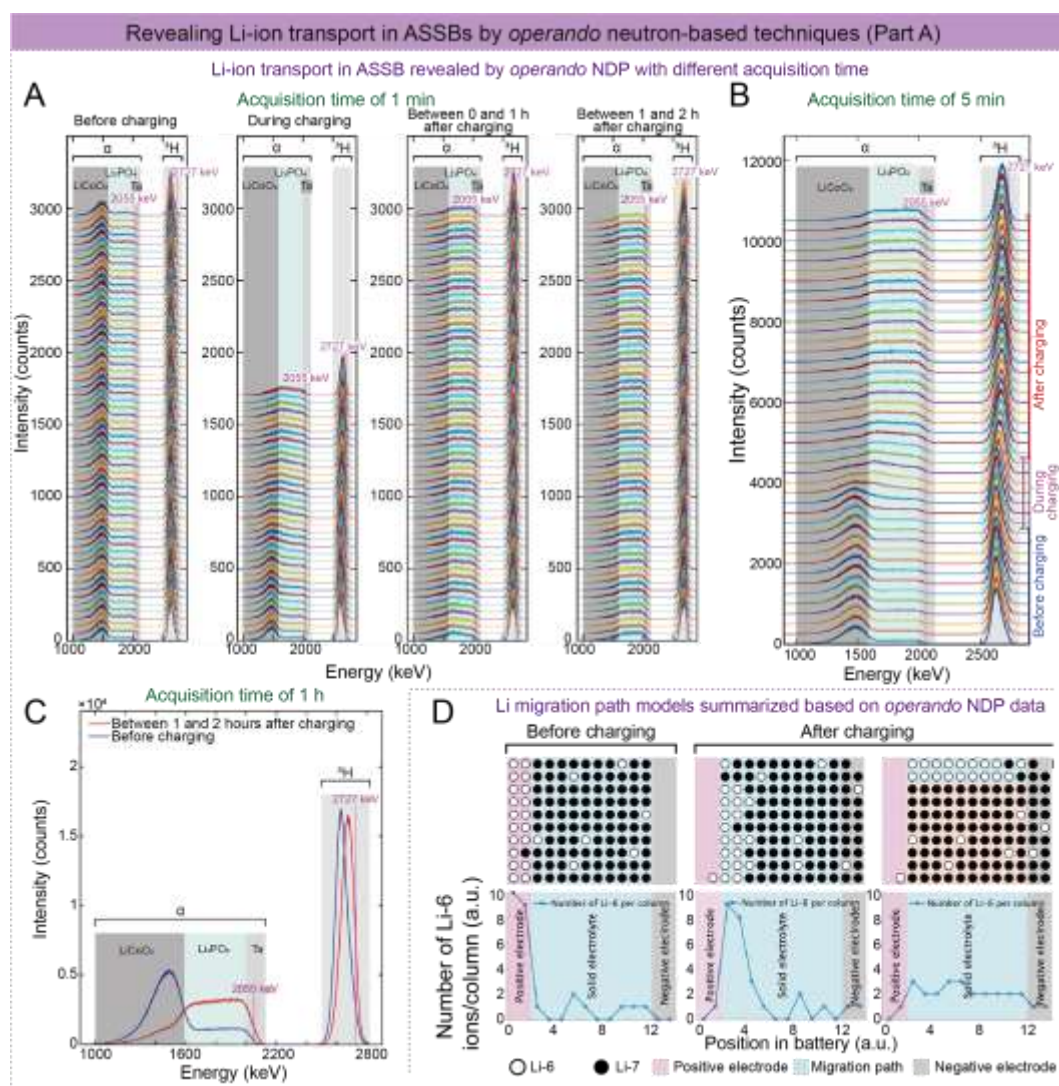


Figure 14. Selected studies on the lithium-ion issues of ASSBs by *operando* neutron-based techniques. Energy spectra of the Pt||LiCoO₂||Li₃PO₄||Ta ASSBs obtained consecutively before, during, and after charging with different acquisition time of (A) 1 min, (B) 5 min, and (C) 1 h; (D) lithium migration path models summarized based on the *operando* NPD data. Reproduced with permission.^[170] Copyright 2022 The Authors, Small published by Wiley-VCH GmbH.

As an important branch of ASSB, all-solid-state lithium-sulfur batteries (ASSLSBs) show great potential to be ideal power source in large-scale applications, due to their high theoretical specific energy, cost effectiveness, and safe operation.^[171-173] However, ASSLSBs have yet to meet performance expectations, which is mainly due to the retarded charge carrier transport dynamics within ionically and electronically insulating sulfur-active materials. Thus, it requires advanced characterization techniques to probe the spatial distribution of transport limitations within cells in real time. In a series of studies, R. Bradbury et al. directly visualized lithium distribution and investigated

lithium-ion transport mechanisms in ASSLSBs using operando neutron imaging (NI).^[174-175] Similar to X-ray imaging technique, NI works by measuring the differences on absorption of neutrons by different materials of the sample, especially for the samples contained light elements.^[19] As shown in **Figure 15A**, a S/C/LPSC||LPSC||In/Li cell encapsulated by a polyimide film and aluminum casting was prepared as the target sample for NI.^[174] The visualization of the lithium distribution at different degrees of discharge (DoDs) during the cell operation is displayed in Figure 15B, where the color scale represents the rate of change in neutron attenuation. It was observed that the maximum rate of attenuation change propagated from the SSE separator side toward the current collector side within the S/C/LPSC cathode as a function of DoD. Beyond vertical lithium distribution (as a function of d), the homo- or heterogenous lithium distributions in the cathode horizontal planes (at a given d) were further investigated by neutron tomography (NT). As displayed in Figure 15C, the cathode side presented a notable difference between the two charge states, which represented the mobile lithium that was stripped from the cathode upon charging. It was also observed that some lithium was trapped and mainly located at the SSE/cathode interface (low d region). Therefore, the presence of a reaction front propagating toward the current collector and a nonuniform reaction in the thickness direction caused by sluggish ion transport of the cathode composite highlighted the necessity of developing high-performance SSEs and optimizing the cathode architectures for ASSLSBs.

Furthermore, the authors continued their efforts to visualize lithium ion transport within the S/C/LPSC||LPSC||In/Li cell by using NI and NT techniques.^[175] Figure 15D shows the evolution of the median neutron attenuation (Σ_{med}) and the change in neutron attenuation ($\Delta\Sigma_{\text{med}}$) at different DoDs along the vertical direction. It was observed that the SSE separator and cathode all exhibited distinct changes in both Σ_{med} and $\Delta\Sigma_{\text{med}}$ across their depth as the cell is discharged, whereas the anode remained almost unchanged in the main part except for a decrease on the side nearest the current collector||anode interface. This was a shift in $^6\text{Li}^+$ ion from the area adjacent to the current collector, where the ^6Li was added during cell assembly, to the area near to the SSE separator. Notably, in the separator region there was a consistent increase in the ^6Li proportion with DoD, especially near the anode interface. Similar to the previous case, lithium distribution changes within horizontal planes were probe by using 3D NT measurements. A quantitative analysis was performed on the evolution of Σ_{med} with DoD in each component. Two key parameters were extracted: the change in Σ_{med} relative

to the 0% DoD ($\Sigma_{\text{med},x} - \Sigma_{\text{med},0}$) and the difference in Σ_{med} between adjacent DoDs ($\Sigma_{\text{med},x} - \Sigma_{\text{med},x-1}$), as presented in Figure 15E. This series of studies provided a relatively comprehensive view about lithium transport dynamics within ASSLSBs, by identifying reaction fronts and lithium concentrations at different DoDs. It was corroborated that the sluggish effective lithium-ion transport in composites cathode is rate-limiting and leads to a nonuniform reaction front, and the limitation is primarily due to the slow ionic transport.

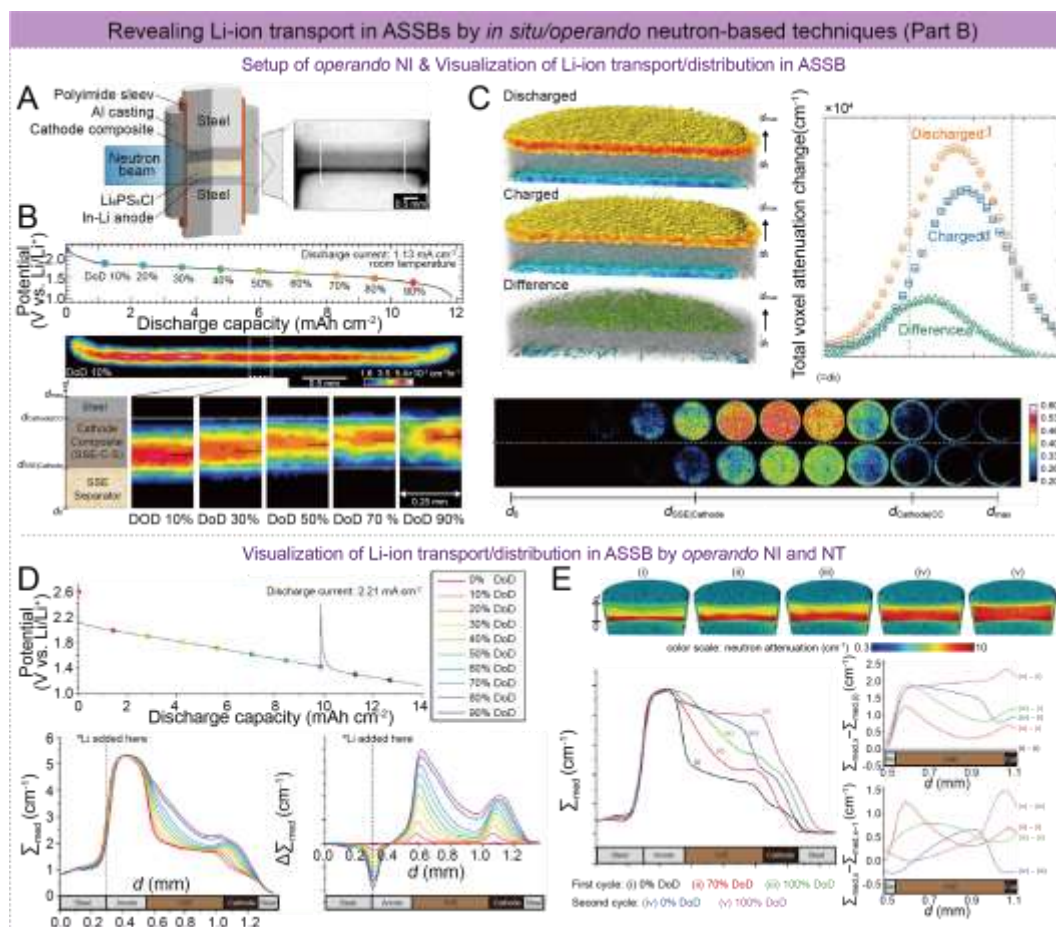


Figure 15. Selected studies on the lithium-ion transport issues of ASSBs by *operando* and *in situ* neutron imaging techniques. (A) Schematic of the neutron imaging setup and corresponding radiography image; (B) *operando* neutron radiography showing lithium distribution dynamics in an S/C/Li₆PS₅Cl||Li₆PS₅Cl||In/Li cell; (C) in situ neutron tomography of discharged and charged solid-state sulfur cathodes. Reproduced with permission.^[174] Copyright 2023 The Authors. Advanced Energy Materials published by Wiley-VCH GmbH. (D) Evolution of median neutron attenuation and its change in the S/C/Li₆PS₅Cl||Li₆PS₅Cl||In/Li cell at different depths of discharge (DoDs); (E) 3D tomography images for each DoD (i–v) showing ⁶Li transport through the cell with corresponding attenuation analysis. Reproduced with permission.^[175] Copyright 2023 The Authors. Advanced Functional Materials published by Wiley-VCH GmbH.

7.2 Electro-chemo-mechanical coupling

Due to solid-solid contacts within ASSBs, phenomena such as material degradation and interface failure often result from a complex interplay of electrochemical, chemical, and mechanical (or physical) factors.^[176-178] Decoupling this complicated relationship and understanding how these factors interact with others in the cell operation is essential to promote development of ASSBs. In the view of methodology, *in situ* and *operando* characterization techniques are highly required to tackle the electro-chemo-mechanical coupling issue since the structural or morphological evolution driven by such multi-field coupling factors is highly time-sensitive.

As an example, F. Sun *et al.* employed *operando* XCT, along with other characterizations and simulations, to decouple the electro-chemo-mechanical coupling in LSPS-based ASSBs with Li-LiAl composite as symmetrical electrodes.^[179] **Figure 16A** presented a set of XCT images of a cell discharged until short-circuit, in which the LSPS SSE displayed a clear structural deformation forming a bowl-like shape with obvious surface cracks. Zoomed-in views revealed interphase regions with lower X-ray absorption at LiAl/LSPS interfaces, which contributed to crack formation. The boundary between Li metal and LiAl alloy shifted toward SSE, and some crack/fissure formed due to the electro-chemo-mechanical coupling. The electrochemical reaction between LSPS and Li metal induced volume shrinkage, and the stress-induced creep deformation of lithium collectively led to the observed volume “expansion” of Li at both electrodes. Due to this mechanical deformation of LSPS, two different LSPS fractures were observed, as shown in Figure 16A-(iii), namely, the irregularly shaped cracks (dark gray areas) and the wedge-like cracks (red diamonds). Furthermore, in a cell after long-term cycling, more cracks were observed within the LSPS SSE by XCT measurement, especially the vertically slit cracks, as displayed in Figure 16B. These slit cracks penetrating the LSPS SSE was responsible for the short-circuit of the cell. The simulation results indicated that the non-uniform electric field distribution would lead to the enhanced reaction of the LSPS neighboring the protrusion part.

D. Cao *et al.* also investigated the electro-chemo-mechanical origins of “soft short” and “creeping” in ASSBs by *operando* NI and XCT measurements.^[180] The so-called “soft short” phenomenon is often observed in ASSBs using Li metal anodes, in which the battery voltage dynamically remains stable but fails to increase during the charging process.^[181-182] However, the

origins of “soft short” have not been well understood yet. In this study, the NCM811||Li_{5.4}PS_{4.4}Cl_{1.6}||Li metal cells were used as the target samples. At first, the “soft short” was studied by *operando* 2D NI, as shown in Figure 16C. In this sequence of NI data, it was observed that the lithium concentration kept increasing during the charging at the anode side, as indicated by the increased black spots, before the “soft short” happened at around 4.5 h. After the “soft short”, the lithium concentration (i.e. the number of black spots) fluctuated, while the voltage also oscillated around 3.8 V. In the cathode side, the increased bright spots demonstrated the depletion of lithium before the “soft short”, and the residual brightness was still observed afterward. This was attributed to the continued Faradic reaction even after the “soft short”. The mentioned evolutions of lithium enrichment and depletion were displayed more vividly in the mapping of neutron transmission intensities, as shown in Figure 16C-(iv) and 16C-(v). The unexpected lithium accumulation was found for stainless steel (SS) electrode, as indicated by the warm-colored peaks at P4 in Figure 16C-(iv) and also in Figure 16C-(v). In this electrochemical inactive region (since the position is distanced from the SSE), the lithium creep toward the SS could be attributed to a combination of stacking pressure and plating-induced compression stress, indicating that the deformation was not exclusively electrochemically induced stress. By further investigation with XCT, as presented in Figure 16D, it was indicated that the existence of low X-ray attenuation filaments (contained pores and inactive lithium) within the LSPC SSE was highly related to the origin of “soft short”. Combined with comprehensive simulation results, the authors proposed an electro-chemo-mechanical reaction-induced mechanism for the lithium deformation and “soft short”, as depicted in Figure 16E. During the initial plating stage, lithium migrated from the cathode and deposited at the interface between the Li metal and the SSE. This resulted in a “soft short,” accompanied by fluctuations in lithium loss and an increase at both the cathode and anode, due to the coupling of mechanical and electrochemical reactions.

These works are typical examples demonstrating the potential to address the electro-chemo-mechanical coupling issues in ASSBs by using powerful *in situ* and *operando* imaging techniques at synchrotron and neutron sources. However, there is still a gap to fully decouple this complexity which is realized by isolating each factor and establishing relationship to structural changes or cell performance. Synchrotron-based multi-modal characterization would be promising to solve this puzzle, which enables simultaneous measurement of both chemical and physical properties of the

sample.

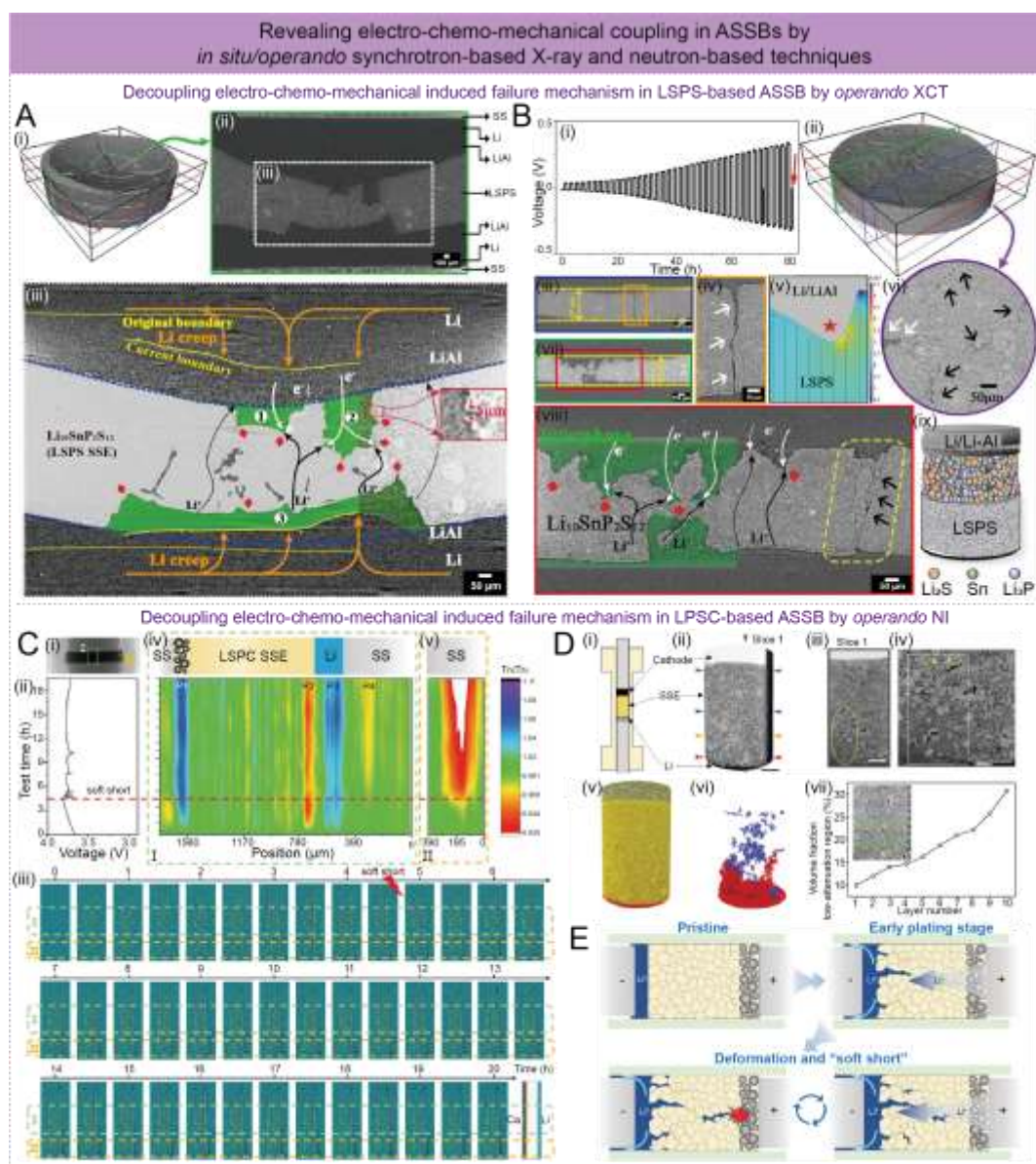


Figure 16. Selected studies on the electro-chemo-mechanical coupling issues of ASSBs by *operando* and *in situ* synchrotron-based X-ray and neutron imaging techniques. (A) XCT characterization results of the Li-LiAl||LSPS||Li-LiAl symmetrical cells after the first discharging until the short circuit; (B) XCT characterization results of the Li-LiAl||LSPS||Li-LiAl symmetrical cells after extended cycling until the short circuit. Reproduced with permission.^[179] Copyright 2022 Wiley-VCH GmbH. (C) *Operando* neutron imaging investigation results of the NCM811||LPSC||Li cells; (D) XCT investigation results of the NCM811||Li_{5.4}PS_{4.4}Cl_{1.6}||Li cells; (E) summarized mechano-electrochemical reactions induced Li deformation and “soft short”. Reproduced with permission.^[180] Copyright 2023 The Authors. Advanced Functional Materials published by Wiley-VCH GmbH.

7.3 Failure and safety

It is generally accepted that ASSBs are much safer than conventional liquid-electrolyte LIBs,

due to the absence of combustible organic liquid electrolytes, which significantly reduces the risk of thermal runaway.^[183] However, whether ASSBs can truly avoid such safety hazards and how to quantitatively determine the safety of ASSBs are still rarely studied. To address these questions, J. Charbonnel *et al.* proposed a methodology to study the thermal runaway of a wide range of ASSBs, involving a closed calorimeter combined with *operando* X-ray imaging.^[184-185] Considering the lack of commercial ASSB products and most lab-fabricated ASSBs have low capacity and low SSE to active materials ratio, which could lead to misrepresentation of reality and overestimation of their safety, the authors modified commercial 18650-type LIB cells (LGHG2) into ASSB cells. These cells composed of graphite/silicon anode, PEO-LLZO SSE, and NCM811 cathode, which had a capacity of 3 Ah and a potential of 4.2 V. For comparison, commercial unmodified LGHG2 cells were used as the reference samples. As presented in **Figure 17A**, the custom-built setup enabled the X-ray radiography during the cell operation and heating, whereas the external conditions, i.e. temperature and pressure, were also monitored by the thermocouples recording (TCR) and pressure recording (PR) sensors, respectively. During the measurements, both the liquid-electrolyte LIB cell and the ASSB cell were continuously heated until the thermal runaway ignition temperature (T_{ini}) was reached, while the X-ray radiography images were collected simultaneously. Figure 17B and 17C present the internal structures of the liquid-electrolyte LIB cell and the ASSB cell, respectively, at moment of T_{ini} (t_{ini}) and at several time points after t_{ini} . According to the continuous observation by X-ray imaging, the thermal runaway process of liquid-electrolyte LIB cell was summarized as illustrated in Figure 17D. The jelly roll collapsed at $t_{ini}+75ms$, and then gas pockets were generated with an electrode assembly delamination at $t_{ini}+120ms$. At $t_{ini}+165ms$, the first particle was evacuated and followed by the successive wave ejections. In contrast, the ASSB cell exhibited a different behavior of thermal runaway. As sketched in Figure 17E, the particle evacuation first occurred at $t_{ini}+80ms$, followed by electrode delamination and jelly roll moving. At $t_{ini}+390ms$, particles and gas were ejected in a single wave, which triggered a large mechanical force turning off the positive pole turn at $t_{ini}+440ms$. By further quantitative analysis, the author concluded that during the thermal runaway, the ASSB cell exhibited a decreased energy release compared to the liquid-electrolyte LIB cell, which could reduce the risk of thermal propagation. Moreover, the gas emission from the ASSB cell was significantly reduced by $40 \pm 20\%$ compared to the liquid-electrolyte LIB cell, potentially lowering toxic gas levels and minimizing the

risk of ATEX (explosive atmospheres). However, the ASSB cell showed a comparable T_{ini} to the liquid-electrolyte LIB cell and reaction kinetics. Therefore, safety issues of ASSBs should receive greater attention and deeper investigation, since currently, the ASSB technologies are not completely safe.

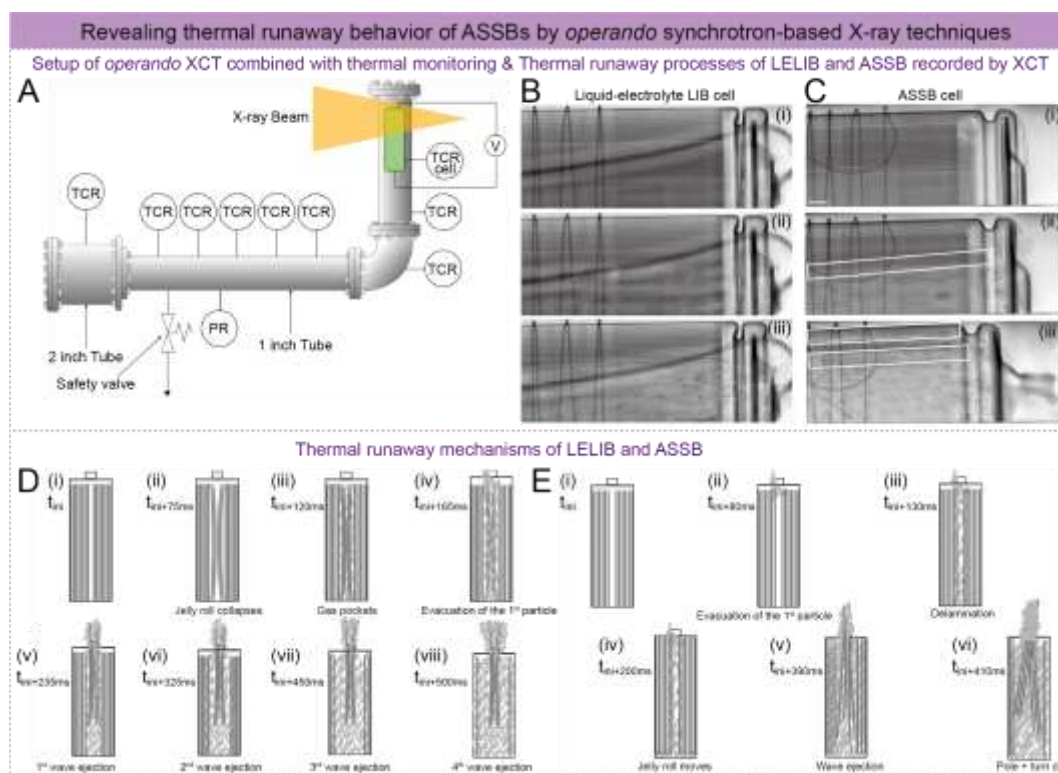


Figure 17. Selected study on the safety issues of ASSBs by *operando* synchrotron-based X-ray imaging technique. (A) Schematic figure of the calorimeter and instrumented cell crossed by the X-ray beam TCR and PR sensors; X-ray radiography of (B) the liquid-electrolyte LIB cell and (C) the ASSB cell during thermal runaway; summarized internal behavior of (D) the liquid-electrolyte LIB cell and (E) the ASSB cell during thermal runaway. Reproduce with permission.^[184] Copyright 2022 American Chemical Society.

8. Conclusion and Perspective

Driven by the highly increasing demand for superior energy density and safety, the transition from traditional LIBs to ASSBs as the next generation of energy storage devices is not only an inevitable result but also urgently needed. Therefore, the challenges and key issues of ASSBs that involve a series of physical, chemical, and mechanical processes need to be well addressed urgently, which depends heavily on the support of advanced characterization techniques. In this review, we specifically focus on *operando* and *in situ* studies using synchrotron-based X-ray and neutron

techniques, revealing the evolution of structures, morphology, and chemical composition at different interfaces within individual components and across entire ASSB cells. **Figure 18** summarizes the *operando* and *in situ* studies discussed in this review by using synchrotron-based X-ray and neutron characterization methods to probe critical issues of ASSBs. The studies conducted at synchrotron sources account for a larger proportion than those conducted at neutron sources, which could be attributed to the higher availability of synchrotron sources and a correspondingly greater accessibility for such studies. Regarding the specific technologies, XCT attracts the most interest and is applied to investigate across nearly all regions of ASSBs (classified in this review) of ASSBs, because of its convenience of providing a direct observation of micro-nano structures in real space. Besides, NDP, XRD, and XANES together share another large part in this statistic, showing their universality and versatility for probing ASSBs. Due to the large scale of subjects, the studies focusing on ASSB cells prefer to use X-ray and neutron imaging techniques. When focusing on the interfaces within ASSBs, various techniques demonstrate strong capabilities on probing the relevant issues. In addition to the extensive applications of synchrotron-based X-ray techniques, neutron-based methods provide a complementary perspective by enabling the detection of lithium transport and distribution within ASSBs. Their integration with synchrotron studies will be essential for achieving a more comprehensive understanding of ASSB materials and interfaces. Looking back at Figure 1, it is evident that these advanced characterization techniques have been applied to address most of the key challenges in ASSBs initially outlined. Although the statistics presented here is only based on a limited number of studies so far, the obtained trends and information about the development of *operando* and *in situ* synchrotron-based X-ray and neutron-based characterization techniques for addressing key challenges in ASSBs are very promising.

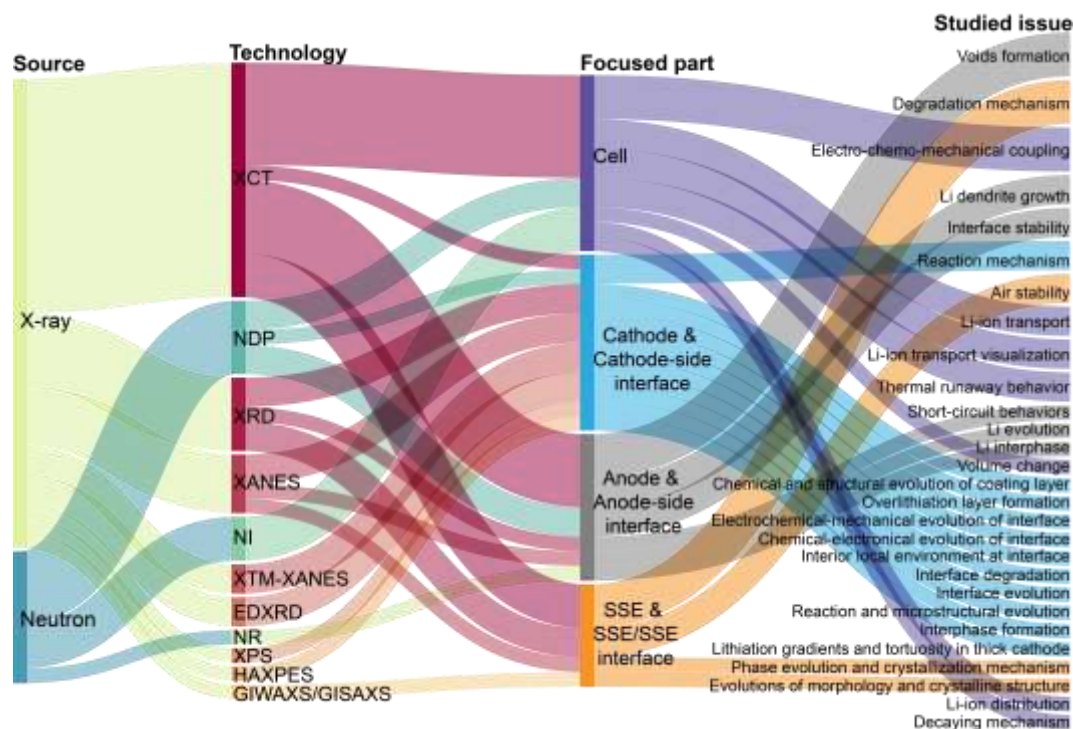


Figure 18. Summary of relevant synchrotron-based X-ray and neutron-based *operando* and *in situ* techniques to probe critical issues of ASSBs, according to the published works in recent five years involved in this review.

To further accelerate the development of ASSBs, synchrotron-based X-ray and neutron-based techniques should also undergo continuous upgrades to meet the various demands. Here, we propose several considerations about how the characterization techniques at synchrotron and neutron sources could evolve in the near future to enhance the ability to solve puzzles related to ASSBs.

(i) Developing multi-modal characterization techniques capable of probing binary and ternary interactions simultaneously are essential to accurately capture the complex interplay of various physical and chemical processes in ASSBs. Considering the complexity inside the ASSBs, especially at the interfaces, a single characterization technique often falls short of revealing the complete evolution of a certain area due to the limited probing type and scale. Some novel multi-modal characterization systems have been available by combining conventional techniques, such as AFM (atomic force microscopy)-IR (infrared spectroscopy), AFM-Raman, and AFM-SEM (scanning electron microscopy)-Raman,^[186-188] but they are rarely reported by using synchrotron-based X-ray and neutron-based techniques. When designing multi-modal characterization systems at synchrotron and neutron sources, compatibility and complementarity between different techniques should be taken into account for a prior consideration. A dual-modal system based on WAXS/SASX (or

GIWAXS/GISAXS) provide strong capability for a wide-range and real-time investigation from the crystalline structure at Å scale to morphology at nm-μm scale of the target sample.^[159, 189-192] For example, M. Povia *et al.* applied operando WAXS/SAXS technique to investigate structural and electrochemical performances of an Na-ion battery.^[189] Transferring the WAXS/SAXS dual-modal characterization from liquid-electrolyte batteries (or other devices) to ASSBs requires a dedicated design of the operando cell and setup. Besides, XRD-CT is also demonstrated as a powerful dual-modal synchrotron-based technique to realize to spatially mapping of a selected crystalline or amorphous phase inside a sample.^[193-197] K. Jensen *et al.* successfully employed the XRD-CT technique to study a LIB and a Ni/MH battery, extracting both structural and morphological (or textural) changes in the battery components.^[194] This pioneering work demonstrated the power of XRD-CT for structural investigations of materials and provided a promising example for further applications in ASSBs.

(ii) Artificial intelligence (AI)-driven pre-experimental screening and post-experimental data processing for the characterizations at synchrotron and neutron sources are expected to make a great difference in the development and popularization of these techniques. AI-based computational methods (including machine learning and big data methods) have already demonstrated their power and utility in high-throughput screening for identifying the most promising materials prior to experimentation,^[198-200] prediction of products and corresponding properties,^[201-204] and mass data processing and preliminary analysis.^[205-206] In particular, massive data sets generated by the ultra-high time or spatial resolution of synchrotron-based X-ray techniques urgently need assistance from AI-based technologies for the data processing to accelerate the analysis.

(iii) On the basis of these two considerations above, an ideal target for synchrotron-based X-ray and neutron-based characterization techniques is establishing a standardized experimental workflow. D. Atkins *et al.* proposed a multiscale and multi-technique integrated workflow of synchrotron-based X-ray and neutron-based characterization techniques for batteries. This framework is based on standardized and automated data acquisition and analysis for high-throughput and high-fidelity experiments, the optimization of versatile and tunable cells, and multi-modal correlative characterization.^[30] Establishing such a workflow is a complicated system engineering that needs multi-cooperation from researchers, beamline scientists and engineers. The aim is to enable a

comprehensive sequence from initial conception and design, selection of characterization technique and set-up, proposal submission, beamtime scheduling, sample preparation, and cell design, preliminary testing, *in situ/operando* experiments proceeding (data acquisition), data analysis, to the final results dissemination. Depending on the number of techniques or even beamlines/sources involved in the workflow, branches of the main sequence also need to be carefully designed and integrated into the overall system. We hope that this review will illuminate how advanced *in situ* and *operando* characterization techniques at synchrotron and neutron sources enable the development of ASSBs by providing detailed and in-depth insights into key challenges, ultimately contributing to their resolution.

Conflicts of Interest

There are no conflicts to declare.

Acknowledgements

This work was supported by funding from the National Natural Science Foundation of China (W2441017; 22409103) and the “Innovation Yongjiang 2035” Key R&D Program (2024Z040, 2025Z063). Y.-J. C. acknowledges the support from Natural Science Foundation of Zhejiang Province (LD22E020003). P. M.-B. acknowledges supports by funding from the Deutsche Forschungsgemeinschaft (DFG, German Research Foundation) under Germany’s Excellence Strategy-EXC 2089/1-390776260 (e-conversion), the International Research Training Group 2022 Alberta/Technical University of Munich International Graduate School for Environmentally Responsible Functional Hybrid Materials (ATUMS), TUM.solar in the context of the Bavarian Collaborative Research Project Solar Technologies Go Hybrid (SolTech), the Center for NanoScience (CeNS) and the China Scholarship Council (CSC).

Received: (will be filled in by the editorial staff)

Revised: (will be filled in by the editorial staff)

Published online: (will be filled in by the editorial staff)

References

- [1] P. P. Lopes, V. R. Stamenkovic, *Science* **2020**, 369, 923.
- [2] J. B. Goodenough, *Acc. Chem. Res.* **2013**, 46, 1053.
- [3] X. Lu, G. Xia, J. P. Lemmon, Z. Yang, *J. Power Sources* **2010**, 195, 2431.
- [4] C. P. Grey, D. S. Hall, *Nat. Commun.* **2020**, 11, 1.
- [5] C. Peng, S. Liang, Y. Yu, L. Cao, C. Yang, X. Liu, K. Guo, P. Müller-Buschbaum, Y. J. Cheng, C. Wang, *Carbon Neutraliz.* **2024**, 1036.
- [6] S. Liang, Y. J. Cheng, J. Zhu, Y. Xia, P. Müller-Buschbaum, *Small Methods* **2020**, 4, 2000218.
- [7] M. Winter, B. Barnett, K. Xu, *Chem. Rev.* **2018**, 118, 11433.
- [8] M. Li, J. Lu, Z. Chen, K. Amine, *Adv. Mater.* **2018**, 30, 1800561.
- [9] T. Schmaltz, F. Hartmann, T. Wicke, L. Weymann, C. Neef, J. Janek, *Adv. Energy Mater.* **2023**, 13, 2301886.
- [10] J. Janek, W. G. Zeier, *Nat. Energy* **2016**, 1, 1.
- [11] L. Xu, S. Tang, Y. Cheng, K. Wang, J. Liang, C. Liu, Y.-C. Cao, F. Wei, L. Mai, *Joule* **2018**, 2, 1991.
- [12] P. Lu, Z. Zhou, Z. Xiao, J. Lu, J. Zhang, G. Hu, W. Yan, S. Xia, S. Zhang, Z. Wang, *Joule* **2024**.
- [13] H.-D. Lim, J.-H. Park, H.-J. Shin, J. Jeong, J. T. Kim, K.-W. Nam, H.-G. Jung, K. Y. Chung, *Energy Storage Mater.* **2020**, 25, 224.
- [14] F. Strauss, D. Kitsche, Y. Ma, J. H. Teo, D. Goonetilleke, J. Janek, M. Bianchini, T. Brezesinski, *Adv. Energy Sustain. Res.* **2021**, 2, 2100004.
- [15] M. Lucero, S. Qiu, Z. Feng, *Carbon Energy* **2021**, 3, 762.
- [16] D. Liu, Z. Shadik, R. Lin, K. Qian, H. Li, K. Li, S. Wang, Q. Yu, M. Liu, S. Ganapathy, *Adv. Mater.* **2019**, 31, 1806620.
- [17] B.-K. Cho, S.-Y. Jung, S.-J. Park, J.-H. Hyun, S.-H. Yu, *ACS Energy Lett.* **2024**, 9, 4068.
- [18] L. Zhang, H. Fan, Y. Dang, Q. Zhuang, H. Arandiyani, Y. Wang, N. Cheng, H. Sun, H. H. P. Garza, R. Zheng, *Mater. Horiz.* **2023**.
- [19] D. Cao, Y. Zhang, T. Ji, H. Zhu, *MRS Bull.* **2023**, 48, 1257.
- [20] F. Tang, Z. Wu, C. Yang, M. Osenberg, A. Hilger, K. Dong, H. Markötter, I. Manke, F. Sun, L. Chen, *Small Methods* **2021**, 5, 2100557.
- [21] S. Lou, N. Sun, F. Zhang, Q. Liu, J. Wang, *Acc. Mater. Res.* **2021**, 2, 1177.
- [22] Y. Xiang, X. Li, Y. Cheng, X. Sun, Y. Yang, *Mater. Today* **2020**, 36, 139.
- [23] J. Janek, W. G. Zeier, *Nat. Energy* **2023**, 8, 230.
- [24] T. Ji, Y. Zhang, J. Torres, A. S. Mijailovic, Y. Tang, X. Zhao, J.-C. Bilheux, J. Wang, B. W. Sheldon, O. Oyediji, H. Zhu, *Nat. Commun.* **2025**, 16, 7667.
- [25] L. Lu, N. Kardjilov, X. Meng, K. Dong, Y. Xu, Q. Wu, A. Tengattini, L. Helfen, J. Yang, Y. Guo, *Adv. Energy Mater.* **2025**, e01324.
- [26] Z. Yu, H. Shan, Y. Zhong, X. Zhang, G. Hong, *ACS Energy Lett.* **2022**, 7, 3151.
- [27] X. Zhang, M. Osenberg, R. F. Ziesche, Z. Yu, J. Kowal, K. Dong, Y. Lu, I. Manke, *ACS Energy Lett.* **2024**, 10, 496.
- [28] A. P. Black, A. Sorrentino, F. Fauth, I. Yousef, L. Simonelli, C. Frontera, A. Ponrouch, D. Tonti, M. R. Palacín, *Chem. Sci.* **2023**, 14, 1641.
- [29] W. Xia, Y. Zhao, F. Zhao, K. Adair, R. Zhao, S. Li, R. Zou, Y. Zhao, X. Sun, *Chem. Rev.* **2022**,

122, 3763.

- [30] D. Atkins, E. Capria, K. Edström, T. Famprakis, A. Grimaud, Q. Jacquet, M. Johnson, A. Matic, P. Norby, H. Reichert, *Adv. Energy Mater.* **2022**, 12, 2102694.
- [31] K. Qian, R. E. Winans, T. Li, *Adv. Energy Mater.* **2021**, 11, 2002821.
- [32] F. Lin, Y. Liu, X. Yu, L. Cheng, A. Singer, O. G. Shpyrko, H. L. Xin, N. Tamura, C. Tian, T.-C. Weng, *Chem. Rev.* **2017**, 117, 13123.
- [33] D. Attwood, *Soft X-rays and Extreme Ultraviolet Radiation: Principles and Applications*, Cambridge University Press, **2000**.
- [34] M. Zhang, Q. Gu, *Chin. Phys. C* **2011**, 35, 1066.
- [35] J. Slater, *Rev. Mod. Phys.* **1948**, 20, 473.
- [36] M. C. García-Gutiérrez, D. R. Rueda, in *Applications of synchrotron Light to Scattering and Diffraction in Materials and Life Sciences*, Springer **2009**, p. 1.
- [37] Y. Lee, E.-S. Kim, J.-G. Hwang, J. Lee, J. Kim, *Nucl. Instrum. Methods Phys. Res. A* **2024**, 1060, 169074.
- [38] S. Mikhailov, V. Litvinenko, M. Busch, M. Emamian, S. Hartman, I. Pinayev, V. Popov, G. Swift, P. Wallace, Y. Wu, presented at Proceedings of the 2003 Particle Accelerator Conference, Portland, USA **2003**.
- [39] C. Wang, T. Ueng, S. Lee, K. Hu, G. Jan, C. Chen, S. Hsu, K. Lin, C. Kuo, K. Hsu, in *International Conference on Accelerator and Large Experimental Physics Control System*, Trieste, Italy 1999.
- [40] A. Balerna, S. Mobilio, in *Synchrotron Radiation: Basics, Methods and Applications*, Springer **2014**, p. 3.
- [41] I. M. Ternov, *Physics-Uspekhi* **1995**, 38, 409.
- [42] K. J. Kim, presented at AIP Conf. Proc., Solapur, India **1989**.
- [43] D. H. Bilderback, P. Elleaume, E. Weckert, *J. Phys. B: At. Mol. Opt. Phys.* **2005**, 38, S773.
- [44] J. R. Helliwell, *Nat. Struct. Biol.* **1998**, 5, 614.
- [45] W. L. Tan, C. R. McNeill, *Appl. Phys. Rev.* **2022**, 9.
- [46] C. Giannini, M. Ladisa, D. Altamura, D. Siliqi, T. Sibillano, L. De Caro, *Crystals* **2016**, 6, 87.
- [47] P. F. Fewster, *X-Ray Scattering from Semiconductors and Other Materials*, World Scientific, **2015**.
- [48] G. Kostorz, in *Physical Metallurgy*, Elsevier **2014**, p. 1227.
- [49] W. Li, M. Li, Y. Hu, J. Lu, A. Lushington, R. Li, T. Wu, T. K. Sham, X. Sun, *Small Methods* **2018**, 2, 1700341.
- [50] P. Sedigh Rahimabadi, M. Khodaei, K. R. Koswattage, *X-Ray Spectrometry* **2020**, 49, 348.
- [51] A. V. Llewellyn, A. Matruglio, D. J. Brett, R. Jervis, P. R. Shearing, *Condensed Matter* **2020**, 5, 75.
- [52] P. Zimmermann, S. Peredkov, P. M. Abdala, S. DeBeer, M. Tromp, C. Müller, J. A. van Bokhoven, *Coord. Chem. Rev.* **2020**, 423, 213466.
- [53] X. Liu, W. Yang, Z. Liu, *Adv. Mater.* **2014**, 26, 7710.
- [54] B.-K. Teo, in *EXAFS Spectroscopy: Techniques and Applications*, Springer **1981**, p. 13.
- [55] X. Li, Z. Ren, M. Norouzi Banis, S. Deng, Y. Zhao, Q. Sun, C. Wang, X. Yang, W. Li, J. Liang, *ACS Energy Lett.* **2019**, 4, 2480.
- [56] M. Wang, L. Árnadóttir, Z. J. Xu, Z. Feng, *Nano-Micro Letters* **2019**, 11, 1.
- [57] Y. Joly, S. Grenier, *X-Ray Absorption and X-Ray Emission Spectroscopy: Theory and Applications* **2016**, 73.

- [58] G. S. Henderson, F. M. De Groot, B. J. Moulton, *Rev. Mineral. Geochem.* **2014**, 78, 75.
- [59] J. Parsons, M. Aldrich, J. Gardea-Torresdey, *Appl. Spectrosc. Rev.* **2002**, 37, 187.
- [60] B.-K. Teo, *Acc. Chem. Res.* **1980**, 13, 412.
- [61] C. Ashley, S. Doniach, *Phys. Rev. B.* **1975**, 11, 1279.
- [62] X. Ou, X. Chen, X. Xu, L. Xie, X. Chen, Z. Hong, H. Bai, X. Liu, Q. Chen, L. Li, *Research* **2021**.
- [63] C. Cao, M. F. Toney, T.-K. Sham, R. Harder, P. R. Shearing, X. Xiao, J. Wang, *Mater. Today* **2020**, 34, 132.
- [64] A. Sakdinawat, D. Attwood, *Nat. Photonics* **2010**, 4, 840.
- [65] J.-Y. Buffiere, E. Maire, J. Adrien, J.-P. Masse, E. Boller, *Exp. Mech.* **2010**, 50, 289.
- [66] J. Baruchel, J.-Y. Buffiere, E. Maire, *X-ray Tomography in Material Science*, Hermes science publications, **2000**.
- [67] P. Pietsch, V. Wood, *Annu. Rev. Mater. Res.* **2017**, 47, 451.
- [68] A. Banerjee, X. Wang, C. Fang, E. A. Wu, Y. S. Meng, *Chem. Rev.* **2020**, 120, 6878.
- [69] F. M. de Groot, E. de Smit, M. M. van Schooneveld, L. R. Aramburo, B. M. Weckhuysen, *ChemPhysChem* **2010**, 11, 951.
- [70] J. W. Stuckey, J. Yang, J. Wang, D. L. Sparks, *J. Environ. Qual.* **2017**, 46, 1166.
- [71] M. Ho, E. Obbard, P. A. Burr, G. Yeoh, *Energy Procedia* **2019**, 160, 459.
- [72] W. M. Stacey, *Nuclear Reactor Physics*, John Wiley & Sons, **2018**.
- [73] J. Wei, H. Chen, Y. Chen, Y. Chen, Y. Chi, C. Deng, H. Dong, L. Dong, S. Fang, J. Feng, *Nucl. Instrum. Methods Phys. Res. A* **2009**, 600, 10.
- [74] G. S. Bauer, *Nucl. Instrum. Methods Phys. Res. A* **2001**, 463, 505.
- [75] P. Lisowski, C. Bowman, G. Russell, S. Wender, *Nucl. Sci. Eng.* **1990**, 106, 208.
- [76] S. Henderson, W. Abraham, A. Aleksandrov, C. Allen, J. Alonso, D. Anderson, D. Arenius, T. Arthur, S. Assadi, J. Ayers, *Nucl. Instrum. Methods Phys. Res. A* **2014**, 763, 610.
- [77] R. Keller, R. Thomae, M. Stockli, R. Welton, presented at AIP Conf. Proc., Yogyakarta, Indonesia **2002**.
- [78] G. Liang, C. Didier, Z. Guo, W. K. Pang, V. K. Peterson, *Adv. Mater.* **2020**, 32, 1904528.
- [79] E. Zhao, Z.-G. Zhang, X. Li, L. He, X. Yu, H. Li, F. Wang, *Chin. Phys. B.* **2020**, 29, 018201.
- [80] M. Abitonze, X. Yu, C. S. Diko, Y. Zhu, Y. Yang, *Batteries* **2022**, 8, 255.
- [81] S. Wang, H. Shi, D. Wang, Y. Xia, Y. Yin, S. Liang, Y. Hu, R. Shao, X. Wu, Z. Xu, *Nano Energy* **2024**, 109337.
- [82] R. F. Ziesche, N. Kardjilov, W. Kockelmann, D. J. Brett, P. R. Shearing, *Joule* **2022**, 6, 35.
- [83] S. Zhe, L. Ming, *Physics* **2024**, 53, 80.
- [84] L. Liu, R. Neuenschwander, A. Rodrigues, *Philos. Trans. R. Soc. A.* **2019**, 377, 20180235.
- [85] A. L. Robinson, *Synchrotron Radiat. News* **2015**, 28, 4.
- [86] M. E. Couprie, *J. Electron. Spectrosc. Relat. Phenom.* **2014**, 196, 3.
- [87] D. Cyranoski, *Nature* **2009**, 459.
- [88] H. Winick, G. P. Williams, *Synchrotron Radiat. News* **1991**, 4, 23.
- [89] H. Winick, *Nucl. Instrum. Methods Phys. Res. A* **1990**, 291, 487.
- [90] M. Shukla, N. Ray, T. Patel, in *Neutron Imaging: Basics, Techniques and Applications*, Springer **2022**, p. 97.
- [91] V. Santoro, K. H. Andersen, D. DiJulio, E. B. Klinkby, T. Miller, D. Milstead, G. Muhrer, M. Strobl, A. Takibayev, L. Zanini, *J. Neutron Res.* **2020**, 22, 209.

- [92] F. Mezei, *C. R. Phys.* **2007**, 8, 909.
- [93] T. E. Mason, M. Arai, K. N. Clausen, *MRS Bull.* **2003**, 28, 923.
- [94] C. Wang, J. Liang, J. T. Kim, X. Sun, *Sci. Adv.* **2022**, 8, eadc9516.
- [95] Y. Liang, H. Liu, G. Wang, C. Wang, Y. Ni, C. W. Nan, L. Z. Fan, *InfoMat* **2022**, 4, e12292.
- [96] H. Bajolle, M. Lagadic, N. Louvet, *Energy Res. Soc. Sci.* **2022**, 93, 102850.
- [97] Y. Yang, E. G. Okonkwo, G. Huang, S. Xu, W. Sun, Y. He, *Energy Storage Mater.* **2021**, 36, 186.
- [98] Y. Zhang, T.-T. Zuo, J. Popovic, K. Lim, Y.-X. Yin, J. Maier, Y.-G. Guo, *Mater. Today* **2020**, 33, 56.
- [99] Z. Luo, X. Qiu, C. Liu, S. Li, C. Wang, G. Zou, H. Hou, X. Ji, *Nano Energy* **2021**, 79, 105507.
- [100] Z. Yu, X. Zhang, C. Fu, H. Wang, M. Chen, G. Yin, H. Huo, J. Wang, *Adv. Energy Mater.* **2021**, 11, 2003250.
- [101] R. Downing, G. Lamaze, J. Langland, S. Hwang, *J. Res. Natl. Inst. Stand. Technol.* **1993**, 98, 109.
- [102] R. G. Downing, G. P. Lamaze, *Neutron News* **1993**, 4, 15.
- [103] J. Oudenhoven, F. Labohm, M. Mulder, R. Niessen, F. Mulder, P. Notten, *Adv. Mater.* **2011**, 35, 4103.
- [104] F. Han, A. S. Westover, J. Yue, X. Fan, F. Wang, M. Chi, D. N. Leonard, N. J. Dudney, H. Wang, C. Wang, *Nat. Energy* **2019**, 4, 187.
- [105] W. Ping, C. Wang, Z. Lin, E. Hitz, C. Yang, H. Wang, L. Hu, *Adv. Energy Mater.* **2020**, 10, 2000702.
- [106] R. Cubitt, G. Fragneto, in *Scattering* (Eds: R. Pike, P. Sabatier), Academic Press, London **2002**, p. 1198.
- [107] J. Daillant, A. Gibaud, *X-Ray and Neutron Reflectivity: Principles and Applications*, Springer, **2008**.
- [108] T. Fears, M. Doucet, J. Browning, J. Baldwin, J. G. Winiarz, H. Kaiser, H. Taub, R. Sacci, G. Veith, *Physical Chemistry Chemical Physics* **2016**, 18, 13927.
- [109] K. L. Browning, A. S. Westover, J. F. Browning, M. Doucet, R. L. Sacci, G. M. Veith, *ACS Energy Lett.* **2023**, 8, 1985.
- [110] Z. Ning, D. S. Jolly, G. Li, R. De Meyere, S. D. Pu, Y. Chen, J. Kasemchainan, J. Ihli, C. Gong, B. Liu, *Nat. Mater.* **2021**, 20, 1121.
- [111] N. Seitzman, O. F. Bird, R. Andrykowski, S. Robbins, M. M. Al-Jassim, S. Pylypenko, *ACS Appl. Energy Mater.* **2021**, 4, 1346.
- [112] W. Li, M. Li, P.-H. Chien, S. Wang, C. Yu, G. King, Y. Hu, Q. Xiao, M. Shakouri, R. Feng, *Sci. Adv.* **2023**, 9, eadh4626.
- [113] L. Auditore, R. Barna, U. Emanuele, D. Loria, A. Trifiro, M. Trimarchi, *Nucl. Instrum. Methods Phys. Res. B.* **2008**, 266, 2138.
- [114] A. du Plessis, S. G. le Roux, A. Guelpa, *Case Stud. Nondestr. Test. Eval.* **2016**, 6, 17.
- [115] P. Pietsch, V. Wood, *Annu. Rev. Mater. Res.* **2017**, 47, 451.
- [116] P. J. Withers, C. Bouman, S. Carmignato, V. Cnudde, D. Grimaldi, C. K. Hagen, E. Maire, M. Manley, A. Du Plessis, S. R. Stock, *Nat. Rev. Methods Primers* **2021**, 1, 18.
- [117] J. Scharf, M. Chouchane, D. P. Finegan, B. Lu, C. Redquest, M.-c. Kim, W. Yao, A. A. Franco, D. Gostovic, Z. Liu, *Nat. Nanotechnol.* **2022**, 17, 446.
- [118] E. P. Alsaç, D. L. Nelson, S. G. Yoon, K. A. Cavallaro, C. Wang, S. E. Sandoval, U. D. Eze,

W. J. Jeong, M. T. McDowell, *Chem. Rev.* **2025**.

- [119] S. Dayani, H. Markötter, A. Schmidt, M. P. Widjaja, G. Bruno, *J. Energy Storage* **2023**, 66, 107453.
- [120] F. S. L. Thomsen, S. Horstmeier, J. H. Niehoff, J. A. Peña, J. Borggreffe, *Invest. Radiol.* **2022**, 57, 620.
- [121] L. Porz, T. Swamy, B. W. Sheldon, D. Rettenwander, T. Frömling, H. L. Thaman, S. Berendts, R. Uecker, W. C. Carter, Y. M. Chiang, *Adv. Energy Mater.* **2017**, 7, 1701003.
- [122] M. Klinsmann, F. E. Hildebrand, M. Ganser, R. M. McMeeking, *J. Power Sources* **2019**, 442, 227226.
- [123] T. Krauskopf, R. Dippel, H. Hartmann, K. Peppler, B. Mogwitz, F. H. Richter, W. G. Zeier, J. Janek, *Joule* **2019**, 3, 2030.
- [124] D. Spencer Jolly, Z. Ning, J. E. Darnbrough, J. Kasemchainan, G. O. Hartley, P. Adamson, D. E. Armstrong, J. Marrow, P. G. Bruce, *ACS Appl. Mater. Interfaces* **2019**, 12, 678.
- [125] J. Kasemchainan, S. Zekoll, D. Spencer Jolly, Z. Ning, G. O. Hartley, J. Marrow, P. G. Bruce, *Nat. Mater.* **2019**, 18, 1105.
- [126] J. A. Lewis, F. J. Q. Cortes, Y. Liu, J. C. Miers, A. Verma, B. S. Vishnugopi, J. Tippens, D. Prakash, T. S. Marchese, S. Y. Han, *Nat. Mater.* **2021**, 20, 503.
- [127] J. Epp, in *Materials Characterization Using Nondestructive Evaluation (NDE) Methods*, Elsevier **2016**, p. 81.
- [128] J. V. Bernier, R. M. Suter, A. D. Rollett, J. D. Almer, *Annu. Rev. Mater. Res.* **2020**, 50, 395.
- [129] A. Iglesias-Juez, G. L. Chiarello, G. S. Patience, M. O. Guerrero-Pérez, *Can. J. Chem. Eng.* **2022**, 100, 3.
- [130] D. Ketenoglu, *X-Ray Spectrometry* **2022**, 51, 422.
- [131] P. Minnmann, F. Strauss, A. Bielefeld, R. Ruess, P. Adelhelm, S. Burkhardt, S. L. Dreyer, E. Trevisanello, H. Ehrenberg, T. Brezesinski, *Adv. Energy Mater.* **2022**, 12, 2201425.
- [132] L. Li, H. Duan, J. Li, L. Zhang, Y. Deng, G. Chen, *Adv. Energy Mater.* **2021**, 11, 2003154.
- [133] K. Hikima, K. Shimizu, H. Kiuchi, Y. Hinuma, K. Suzuki, M. Hirayama, E. Matsubara, R. Kanno, *J. Am. Chem. Soc.* **2021**, 144, 236.
- [134] J. F. Watts, J. Wolstenholme, *An Introduction to Surface Analysis by XPS and AES*, John Wiley & Sons, **2019**.
- [135] J. Chastain, R. C. King Jr, *Handbook of X-ray Photoelectron Spectroscopy*, **1992**.
- [136] B. Philippe, M. Hahlin, K. Edström, T. Gustafsson, H. Siegbahn, H. Rensmo, *J. Electrochem. Soc.* **2015**, 163, A178.
- [137] W. Hou, X. Guo, X. Shen, K. Amine, H. Yu, J. Lu, *Nano Energy* **2018**, 52, 279.
- [138] B. Pandit, M. Johansen, C. Susana Martínez-Cisneros, J. M. Naranjo-Balseca, B. Levenfeld, D. B. Ravnsbæk, A. Varez, *Chem. Mater.* **2024**.
- [139] S. Su, J. Ma, L. Zhao, K. Lin, Q. Li, S. Lv, F. Kang, Y. B. He, *Carbon Energy* **2021**, 3, 866.
- [140] N. Li, J. Luo, J. Zhu, X. Zhuang, *Energy Storage Mater.* **2023**, 103034.
- [141] S. Deng, Q. Sun, M. Li, K. Adair, C. Yu, J. Li, W. Li, J. Fu, X. Li, R. Li, *Energy Storage Mater.* **2021**, 35, 661.
- [142] R. Gao, L. Zhang, F. Tao, J. Wang, G. Du, T. Xiao, B. Deng, *Analyst* **2024**, 149, 4506.
- [143] Y. Xie, H. Wang, G. Xu, J. Wang, H. Sheng, Z. Chen, Y. Ren, C. J. Sun, J. Wen, J. Wang, *Adv. Energy Mater.* **2016**, 6, 1601306.
- [144] N. Sun, Q. Liu, Y. Cao, S. Lou, M. Ge, X. Xiao, W.-K. Lee, Y. Gao, G. Yin, J. Wang, X. Sun,

Angew. Chem., Int. Ed. **2019**, 58, 18647.

- [145] X. Sun, A. M. Stavola, D. Cao, A. M. Bruck, Y. Wang, Y. Zhang, P. Luan, J. W. Gallaway, H. Zhu, *Adv. Energy Mater.* **2021**, 11, 2002861.
- [146] B. Kämpfe, F. Luczak, B. Michel, *Part. Part. Syst. Charact.* **2005**, 22, 391.
- [147] J. L. Provis, J. S. Van Deventer, *Chem. Eng. Sci.* **2007**, 62, 2309.
- [148] A. Sakuda, A. Hayashi, T. Ohtomo, S. Hama, M. Tatsumisago, *J. Power Sources* **2011**, 196, 6735.
- [149] J. H. Woo, J. E. Trevey, A. S. Cavanagh, Y. S. Choi, S. C. Kim, S. M. George, K. H. Oh, S.-H. Lee, *J. Electrochem. Soc.* **2012**, 159, A1120.
- [150] Y. Ito, Y. Sakurai, S. Yubuchi, A. Sakuda, A. Hayashi, M. Tatsumisago, *J. Electrochem. Soc.* **2015**, 162, A1610.
- [151] K. Takada, N. Ohta, Y. Tateyama, *J. Inorg. Organomet. Polym. Mater.* **2015**, 25, 205.
- [152] Y. Zhao, L. Zhang, J. Liu, K. Adair, F. Zhao, Y. Sun, T. Wu, X. Bi, K. Amine, J. Lu, *Chem. Soc. Rev.* **2021**, 50, 3889.
- [153] X. Liu, Y. Cheng, Y. Su, F. Ren, J. Zhao, Z. Liang, B. Zheng, J. Shi, K. Zhou, Y. Xiang, *Energy Storage Mater.* **2023**, 54, 713.
- [154] P. Albertus, V. Anandan, C. Ban, N. Balsara, I. Belharouak, J. Buettner-Garrett, Z. Chen, C. Daniel, M. Doeff, N. J. Dudney, *ACS Energy Lett.* **2021**, 6, 1399.
- [155] M. Dixit, A. Parejiya, R. Essehli, N. Muralidharan, S. U. Haq, R. Amin, I. Belharouak, *Cell Rep. Phys. Sci.* **2022**, 3.
- [156] A. M. Stavola, X. Sun, D. P. Guida, A. M. Bruck, D. Cao, J. S. Okasinski, A. C. Chuang, H. Zhu, J. W. Gallaway, *ACS Energy Lett.* **2023**, 8, 1273.
- [157] H. Zhu, T. Ji, Y. Zhang, J. Torres, J. Bilheux, J. Wang, **2024**.
- [158] W. Li, J. Liang, M. Li, K. R. Adair, X. Li, Y. Hu, Q. Xiao, R. Feng, R. Li, L. Zhang, *Chem. Mater.* **2020**, 32, 7019.
- [159] Y. Liang, T. Zheng, K. Sun, Z. Xu, T. Guan, F. A. Apfelbeck, P. Ding, I. D. Sharp, Y. Cheng, M. Schwartzkopf, S. V. Roth, P. Müller-Buschbaum, *ACS Appl. Mater. Interfaces* **2024**.
- [160] P. Müller-Buschbaum, *Anal. Bioanal. Chem.* **2003**, 376, 3.
- [161] P. Müller-Buschbaum, *Adv. Mater.* **2014**, 26, 7692.
- [162] J. A. Lewis, F. J. Q. Cortes, M. G. Boebinger, J. Tippens, T. S. Marchese, N. Kondekar, X. Liu, M. Chi, M. T. McDowell, *ACS Energy Lett.* **2019**, 4, 591.
- [163] Y. Morino, H. Tsukasaki, S. Mori, *ACS Appl. Mater. Interfaces* **2023**, 15, 23051.
- [164] J. Tippens, J. C. Miers, A. Afshar, J. A. Lewis, F. J. Q. Cortes, H. Qiao, T. S. Marchese, C. V. Di Leo, C. Saldana, M. T. McDowell, *ACS Energy Lett.* **2019**, 4, 1475.
- [165] M. B. Dixit, N. Singh, J. P. Horwath, P. D. Shevchenko, M. Jones, E. A. Stach, T. S. Arthur, K. B. Hatzell, *Matter* **2020**, 3, 2138.
- [166] X. Li, J. Liang, N. Chen, J. Luo, K. R. Adair, C. Wang, M. N. Banis, T. K. Sham, L. Zhang, S. Zhao, *Angew. Chem.* **2019**, 131, 16579.
- [167] L. Zhou, C. Y. Kwok, A. Shyamsunder, Q. Zhang, X. Wu, L. F. Nazar, *Energy Environ. Sci.* **2020**, 13, 2056.
- [168] L. Ye, X. Li, *Nature* **2021**, 593, 218.
- [169] B. Hu, S. Zhang, Z. Ning, D. Spencer-Jolly, D. L. Melvin, X. Gao, J. Perera, S. D. Pu, G. J. Rees, L. Wang, *Joule* **2024**.
- [170] T. Kobayashi, T. Ohnishi, T. Osawa, A. Pratt, S. Tear, S. Shimoda, H. Baba, M. Laitinen, T.

- Sajavaara, *Small* **2022**, 18, 2204455.
- [171] J. T. Kim, H. Su, Y. Zhong, C. Wang, H. Wu, D. Zhao, C. Wang, X. Sun, Y. Li, *Nat. Chem. Eng.* **2024**, 1, 400.
- [172] J. T. Kim, X. Hao, C. Wang, X. Sun, *Matter* **2023**, 6, 316.
- [173] J. T. Kim, A. Rao, H.-Y. Nie, Y. Hu, W. Li, F. Zhao, S. Deng, X. Hao, J. Fu, J. Luo, *Nat. Commun.* **2023**, 14, 6404.
- [174] R. Bradbury, G. F. Dewald, M. A. Kraft, T. Arlt, N. Kardjilov, J. Janek, I. Manke, W. G. Zeier, S. Ohno, *Adv. Energy Mater.* **2023**, 13, 2203426.
- [175] R. Bradbury, N. Kardjilov, G. F. Dewald, A. Tenggattini, L. Helfen, W. G. Zeier, I. Manke, *Adv. Funct. Mater.* **2023**, 33, 2302619.
- [176] J. Tian, Z. Chen, Y. Zhao, *ACS Omega* **2022**, 7, 6455.
- [177] P. Wang, W. Qu, W. L. Song, H. Chen, R. Chen, D. Fang, *Adv. Funct. Mater.* **2019**, 29, 1900950.
- [178] Y. Zhong, X. Zhang, Y. Zhang, P. Jia, Y. Xi, L. Kang, Z. Yu, *SusMat* **2024**, 4, e190.
- [179] F. Sun, C. Wang, M. Osenberg, K. Dong, S. Zhang, C. Yang, Y. Wang, A. Hilger, J. Zhang, S. Dong, *Adv. Energy Mater.* **2022**, 12, 2103714.
- [180] D. Cao, K. Zhang, W. Li, Y. Zhang, T. Ji, X. Zhao, E. Cakmak, J. Zhu, Y. Cao, H. Zhu, *Adv. Funct. Mater.* **2023**, 33, 2307998.
- [181] M. J. Counihan, K. S. Chavan, P. Barai, D. J. Powers, Y. Zhang, V. Srinivasan, S. Tepavcevic, *Joule* **2024**, 8, 64.
- [182] C. Wang, T. Deng, X. Fan, M. Zheng, R. Yu, Q. Lu, H. Duan, H. Huang, C. Wang, X. Sun, *Joule* **2022**, 6, 1770.
- [183] W. Huang, X. Feng, X. Han, W. Zhang, F. Jiang, *Cell Rep. Phys. Sci.* **2021**, 2.
- [184] J. Charbonnel, N. Darmet, C. Deilhes, L. Broche, M. Reytyer, P.-X. Thivel, R. Vincent, *ACS Appl. Energy Mater.* **2022**, 5, 10862.
- [185] J. Charbonnel, S. Dubourg, E. Testard, L. Broche, C. Magnier, T. Rochard, D. Marteau, P.-X. Thivel, R. Vincent, *Iscience* **2023**, 26.
- [186] A. Dazzi, C. B. Prater, *Chem. Rev.* **2017**, 117, 5146.
- [187] P. Beekman, A. Enciso-Martinez, H. S. Rho, S. P. Pujari, A. Lenferink, H. Zuilhof, L. W. Terstappen, C. Otto, S. Le Gac, *Lab Chip* **2019**, 19, 2526.
- [188] J. C. Fernandes, V. Mareau, L. Gonon, *Int. J. Polym. Anal. Charact.* **2018**, 23, 113.
- [189] M. Povia, J. Sottmann, G. Portale, K. D. Knudsen, S. Margadonna, S. Sartori, *J. Phys. Chem, C* **2018**, 122, 5917.
- [190] X. Liu, S.-C. Lee, S. Seifer, R. E. Winans, L. Cheng, T. Li, *Energy Storage Mater.* **2022**, 45, 696.
- [191] G. Greco, G. A. Elia, D. Hermida-Merino, R. Hahn, S. Raoux, *Small methods* **2023**, 7, 2201633.
- [192] S. Liang, T. Guan, S. Yin, S. Tu, R. Guo, Y. Bulut, K. A. Reck, J. Drewes, W. Chen, T. Strunskus, *Nanoscale Horiz.* **2024**, 9, 2273.
- [193] G. Artioli, T. Cerulli, G. Cruciani, M. C. Dalconi, G. Ferrari, M. Parisatto, A. Rack, R. Tucoulou, *Anal. Bioanal. Chem.* **2010**, 397, 2131.
- [194] K. M. Jensen, X. Yang, J. V. Laveda, W. G. Zeier, K. A. See, M. Di Michiel, B. C. Melot, S. A. Corr, S. J. Billinge, *J. Electrochem. Soc.* **2015**, 162, A1310.
- [195] H. Liu, S. Kazemiabnavi, A. Grenier, G. Vaughan, M. Di Michiel, B. J. Polzin, K. Thornton,

- K. W. Chapman, P. J. Chupas, *ACS Appl. Mater. Interfaces* **2019**, 11, 18386.
- [196] V. Middelkoop, A. Vamvakeros, D. De Wit, S. D. Jacques, S. Danaci, C. Jacquot, Y. De Vos, D. Matras, S. W. Price, A. M. Beale, *J. CO₂ Util.* **2019**, 33, 478.
- [197] S. W. Price, A. Van Loon, K. Keune, A. D. Parsons, C. Murray, A. M. Beale, J. F. W. Mosselmans, *Chem. Commun.* **2019**, 55, 1931.
- [198] X. Rodríguez-Martínez, E. Pascual-San-José, M. Campoy-Quiles, *Energy Environ. Sci.* **2021**, 14, 3301.
- [199] J. M. Gregoire, L. Zhou, J. A. Haber, *Nat. Synth.* **2023**, 2, 493.
- [200] J. Benavides-Hernández, F. Dumeignil, *ACS Catal.* **2024**, 14, 11749.
- [201] N. Ninduwezuor-Ehiobu, O. A. Tula, C. Daraojimba, K. A. Ofonagoro, O. A. Ogunjobi, J. O. Gidiagba, B. A. Egbokhaebho, A. A. Banso, *Eng. Sci. Technol. Int. J.* **2023**, 4, 66.
- [202] S. Prateek, R. Garg, K. Kumar Saxena, V. Srivastav, H. Vasudev, N. Kumar, *Adv. Mater. Process. Technol.* **2024**, 10, 708.
- [203] Y.-F. Tu, M.-Y. Kwan, K.-L. Yick, *Materials* **2024**, 17, 5009.
- [204] X. Wang, B. He, B. Liu, M. Avdeev, S. Shi, *Adv. Funct. Mater.* **2024**, 2406146.
- [205] Z. Ma, S. Kim, P. Martínez-Gómez, J. Taghia, Y.-Z. Song, H. Gao, *IEEE Access* **2020**, 8, 199882.
- [206] M. Tipaldi, L. Feruglio, P. Denis, G. D'Angelo, *Annu. Rev. Control.* **2020**, 49, 197.